SIAM J. IMAGING SCIENCES
Vol. 0, No. 0, pp. 000–000


# Low-Frequency Electromagnetic Imaging Using Sensitivity Functions and Beamforming*

Pierre-David Letourneau[†], Mitchell Tong Harris[‡], Matthew Harper Langston[‡], and George Papanicolaou[§]

**Abstract.** We present a computational technique for low-frequency electromagnetic imaging in inhomogeneous media that provides superior three-dimensional resolution over existing techniques. The method is enabled through large-scale, fast (low-complexity) algorithms that we introduce for simulating electromagnetic wave propagation. We numerically study the performance of the technique on various problems including the imaging of a strong finite scatterer located within a thick conductive box.

**Key words.** imaging, Maxwell's equations, low frequency, VLF/ELF, computational imaging

**AMS subject classifications.** 78-04, 65R32, 35H99, 65T50

**DOI.** 10.1137/19M1279502

## 1. Introduction.

Imaging through conductive structures embedded in a dielectric medium, such as air/sea water or air/metal containers, using electromagnetic waves is generally considered a difficult problem. On one hand, existing high-frequency techniques are theoretically well understood, provide resolution guarantees, and can be used in combination with efficient algorithms. On the other hand, high-frequency methods cannot be employed in this context because high-frequency waves do not penetrate deeply enough within conductive structures to produce a signal containing sufficient information for imaging purposes. Low-frequency waves, on the other hand, have a much superior penetrating power. Further, they can propagate through dielectric media, which is a feat not achievable by DC signals (frequency $\omega = 0$), as they are are limited to purely conductive material. Unfortunately, existing low-frequency techniques exhibit low resolution and incur such a high computational cost that they are of little practical use.

In this context, we present a novel scheme for performing imaging using low-frequency electromagnetic waves. Wavelengths under consideration are orders-of-magnitude larger than the imaging domain, and can be generated with ease using recently developed portable sources [30].

*Received by the editors August 7, 2019; accepted for publication (in revised form) February 13, 2020; published electronically DATE.
https://doi.org/10.1137/19M1279502
**Funding:** The work of the authors was supported by the Defense Advanced Research Projects Agency (DARPA) ITA3 (Imaging Through Almost Anything Anywhere) Disruption Opportunity under grant HR001118C0048. Any opinions, findings and conclusions or recommendations expressed in this material are those of the authors and do not necessarily reflect the views, the official policy or position of the Department of Defense or the U.S. Government. Distribution Statement A (Approved for Public Release, Distribution Unlimited).
[†]Corresponding author. Reservoir Labs, New York, NY 10012 (letourneau@reservoir.com).
[‡]Reservoir Labs, New York, NY 10012 (mitchell.harris@mit.edu, langston@reservoir.com).
[§]Department of Mathematics, Stanford University, Stanford, CA 94305 (papanicolaou@stanford.edu).

The method relies on a novel computational filtering scheme (section 1.4), and its application at practical scales is made possible only through the use of state-of-the-art fast algorithms for simulating electromagnetic signals in complex media, which we introduce. It can achieve significantly higher resolution than existing low-frequency techniques. It also possesses higher imaging capabilities than high-frequency methods in media involving conductive materials and is highly versatile.

The paper is structured as follows: the remainder of this section describes existing techniques and gives an overview of our proposed method and contributions. Section 2 details the physical model as well as the theoretical tools underlying the imaging technique. Section 3 provides information about the fast algorithm used to perform physical simulations. The imaging algorithm specifics can be found in section 4, and extensive numerical results are presented in section 5.

**1.1. Related material.** There are three commonly employed low-frequency electromagnetic imaging methods related to the one we present here: (1) electrical impedance tomography (EIT) (also known as electrical resistance tomography [6, 18, 49]), (2) electrical capacitance tomography (ECT) [14, 45, 52], and (3) magnetic induction tomography (MIT) (also known as mutual inductance tomography, or electromagnetic tomography [1, 25, 35]).

All aforementioned techniques are based on Maxwell's equations (7) but rely on different sets of modeling assumptions and approximations: EIT (section 1.2.1) is essentially a zero-frequency approximation ($\omega = 0$) that uses potentials and direct current injections to recover the conductivity ($\sigma$). ECT, discussed in section 1.2.2, is designed to recover permittivity ($\epsilon$) distributions in insulating materials through capacitance measurements. Finally, MIT (section 1.2.3) is based on a low-frequency ($\omega \approx 0$) approximation that uses alternating currents and field measurements to produce an image of low-permittivity materials. Under appropriate circumstances, e.g., when the skin depth of an inclusion is comparable to its characteristic size [1], it has the ability to identify both permeability ($\mu$) and conductivity ($\sigma$) perturbations.

The method presented in this paper does not make any such modeling assumptions or approximations. Rather, our methodology is based on solutions of the complete system of Maxwell's equations, and thus it can capture all possible phenomena, can treat complex materials, and can recover permittivity ($\epsilon$), conductivity ($\sigma$), and permeability ($\mu$) perturbations. As noted in Griffiths [25], such considerations of the full electromagnetic wave propagation problem are of prime importance, especially in biomedical applications. Below, we provide further details regarding each technique and discuss recent highlights of the literature on each topic.

**1.2. Physical modeling and low-frequency imaging techniques.** We now describe the most common low-frequency imaging techniques, as well as their advantages and their limitations.

**1.2.1. Electrical impedance tomography.** EIT is used to recover an unknown conductivity distribution $\sigma(x)$ from boundary measurements. The governing system of equations of

EIT under the complete electrode model [18, 41]) takes the following form:

$$
\begin{aligned}
-\nabla \cdot (\sigma(x)\, \nabla u(x)) &= 0, \qquad x \in \Omega,\\
\int_{e_k} \sigma\, \frac{\partial u}{\partial \hat{n}}\, \mathrm{d}s &= I_k, \qquad k = 1, \dots, K,\\
\sigma(x)\, \frac{\partial u}{\partial \hat{n}}(x) &= 0 \qquad \forall\ x \in \partial\Omega \setminus \cup_{k=1}^{K} e_k,\\
u(x) + z_k\, \sigma(x)\, \frac{\partial u}{\partial \hat{n}}(x) &= V_k \qquad \forall\ x \in e_k,\ k = 1, \dots, K,
\end{aligned}
\tag{1}
$$

where $\Omega \in \mathbb{R}^d$ $(d = 2, 3)$ is an open domain with Lipschitz boundary $\partial\Omega$, $\hat{n}$ is the unit normal vector on $\partial\Omega$, $\sigma(x)$ is the conductivity distribution to be recovered, $\{e_k\}$ are boundary sets representing the location area of electrodes, $u(x)$ is the electric potential, $\{z_k\}$ are contact impedances, $\{V_k\}$ are known applied potentials at the boundary, and $\{I_k\}$ are known currents applied at the boundary.[1] The partial differential equation (PDE) system is of an elliptic nature and can be derived under a quasi-static assumption on the electromagnetic process [23, 41]. In particular, EIT is restricted by the fact that the medium under consideration must be conductive. In this sense, it applies to fields such as medical imaging, nondestructive testing, and geophysical prospecting but leaves out applications such as target localization in air or underwater imaging in the presence of an air/water interface. EIT has been extensively studied theoretically and numerically. From a theoretical standpoint, we refer the reader to Borcea [6] and Uhlmann [49] for a survey of existence, uniqueness, and regularity results. Cui et al. [14] also provide a good overview of numerical methods for EIT. Numerical imaging algorithms are also discussed in section 1.3.

**1.2.2. Electrical capacitance tomography.** ECT [14, 44, 52] is a method used to recover a permittivity distribution $\epsilon(x)$ within an insulator. It is mathematically similar to EIT, with a governing system of PDEs given by

$$
\begin{aligned}
-\nabla \cdot (\epsilon(x)\, \nabla u(x)) &= 0, \qquad x \in \Omega,\\
\int_{e_k} \epsilon\, \frac{\partial u}{\partial \hat{n}}\, \mathrm{s} &= Q_k, \qquad k = 1, \dots, K,\\
u(x) &= 0 \qquad \forall\ x \in \partial\Omega \setminus \cup_{k=1}^{K} e_k,\\
u(x) &= V_k \qquad \forall\ x \in e_k,\ k = 1, \dots, K,
\end{aligned}
\tag{2}
$$

where $\Omega \in \mathbb{R}^d$ $(d = 2, 3)$ is, again, an open domain with Lipschitz boundary $\partial\Omega$, $\epsilon(x)$ is the permittivity distribution to be recovered, $\{e_k\}$ are boundary sets representing the location area of electrodes (sources/receivers), $u(x)$ is the electric potential, $\{V_k\}$ are known applied potentials at the boundary, and $\{Q_k\}$ are the total electric charges on the portions $\{e_k\}$ of

[1] The solution map from boundary potentials to currents on the boundary is generally referred to as the Dirichlet-to-Neumann map, whereas the map from currents to potentials is called the Neumann-to-Dirichlet map (NtD).

the boundary. The PDE system is elliptic like that of EIT. In the absence of a charge density, it can be derived from Maxwell's equations under the assumption that the medium is non-conducting ($\sigma = 0$) and of sufficiently low permeability relative to the frequency being used ($\omega\mu \approx 0$). For a recent survey of applications and imaging techniques in ECT, we refer the reader to Cui et al. [14].

**1.2.3. Magnetic induction tomography.** MIT relies on the following PDE system, sometimes referred to as the eddy current equations [1, 25, 35, 38]:

$$\nabla \times E(x) = i\omega\mu(x)H(x), \quad x \in \mathbb{R}^3, \tag{3}$$

$$\nabla \times H(x) = \sigma(x)E(x) + J(x), \quad x \in \mathbb{R}^3, \tag{4}$$

$$E(x) = O\left(|x|^{-1}\right), \ \ H(x) = O\left(|x|^{-1}\right), \quad |x| \to \infty, \tag{5}$$

where $E(x)$ is the electric field, $H(x)$ is the magnetic field, $J(x)$ are external electric currents, $\sigma(x)$ is a conductivity distribution, $\mu(x)$ is a permeability distribution, and $\omega$ is the working angular frequency (time harmonic). This system of PDEs is of a diffusive nature. It can be obtained as a first-order approximation of Maxwell's equations at low frequency [32, eq. 2], or under an assumption of low permittivity relative to frequency ($\omega\epsilon \ll 1$) [38]. It uses low-frequency alternating magnetic fields to probe the medium. MIT has found applications in both the industrial [37] and the biomedical fields [24, 34]. One practical advantage of MIT is that it does not require direct contact with the medium (as opposed to EIT where such contact leads to impedance). Further, it is sensitive to both the permeability ($\mu$) and the conductivity ($\sigma$) of the medium.

**1.3. Image reconstruction techniques and algorithms.** Despite different underlying models, the aforementioned imaging methods make use of similar image reconstruction techniques. Here, we provide a brief description of the most commonly used algorithms.

*Output least squares* [6, 9, 15, 16, 20, 21, 23] is by far the most commonly employed technique. It relies on an optimization problem of the form $\min_{\delta\sigma} ||F(\sigma)\,\delta\sigma - g||_2^2 + P\,(\delta\sigma)$, where $F$ is the forward modeling operator, $\delta\sigma$ is the quantity to be imaged, $g$ are the measured data, and $P\,(\cdot)$ is a regularizing term. There are various possible choices for $P\,(\cdot)$. Examples include (1) $P\,(\delta\sigma) = ||\delta\sigma||_2^2$ (Tikhonov) [23, 47] which can overcome underdeterminess but leads to resolution loss, (2) $P\,(\delta\sigma) = ||\delta\sigma||_1$ [20, 21, 23, 29] which promotes sparsity in the image, and (3) $P\,(\delta\sigma) = ||\delta\sigma||_{TV}$ [10, 23] (total variation) which promotes sparsity and sharp edges in the image. Output least-squares methods are computationally advantageous thanks to the existence of efficient algorithms for the application of the various operators involved. Their main drawback is associated with the nonlinear nature of the inverse problem that can lead descent schemes towards erroneous images (local minimum).

We underline that the technique presented in this paper belongs to this category. However, the regularization technique (filtering, section 4) employed is different from those listed above and, to the authors' knowledge, completely novel in this context.

*Variational methods (EIT and ECT only)* [2, 6] are based on variational principles. They represent powerful tools for the theoretical study of the EIT and ECT problems [19]. However, from a numerical standpoint, their direct application for image reconstruction has proved elusive, either due to ill-conditioning, lack of regularity, or lack of uniqueness [6, 31]. Nonetheless, using variational-principles-like equations as constraints on optimization-based inversion scheme has shown promise [5, 8].

*Bayesian inversion methods* [17, 18] attempt to recover the posterior distribution of some material properties given the data $g$, i.e., $\mathbb{P}\left(\sigma|\, g\right) = \frac{\mathbb{P}(g|\sigma)\,\mathbb{P}(\sigma)}{\mathbb{P}(g)}$. To do so, a forward and measurement noise models are used, together with a (user-provided) prior distribution. Once a posterior distribution of the properties has been constructed, its mean is generally taken as the solution of the inverse problem. Theoretical correctness and stability of the Bayesian inverse problem have recently been studied in Dunlop and Stuart [18]. Bayesian inverse methods are both versatile and well suited for uncertainty quantification. However, they are also computationally expensive, requiring a very large number of simulations in order to reach convergence (Markov chain Monte Carlo [11]). Further, the inversion process can be highly sensitive to the choice of prior distribution as shown in Dunlop and Stuart [18].

*Monoticity-based methods (EIT and ECT only)* [22, 27, 43, 44] take their name from the fact that if $\sigma(x)$ and $\tau(x)$ are two conductivity distributions and if $\Lambda_{NtD}(\cdot)$ represents the NtD map [27], then $\sigma(x) \leq \tau(x) \;\Rightarrow\; \Lambda_{NtD}(\sigma) \succeq \Lambda_{NtD}(\tau)$. To proceed to the inversion, one visits every voxel in the image, perturbs it, solves the perturbed problem, and verifies whether $\Lambda_{NtD}(\sigma) \succeq \Lambda_{NtD}(\tau)$, thus establishing whether the current voxels overlaps with a region of higher conductivity. If so, the voxel is “included in the image.” Otherwise, one moves to the next voxel. One advantage of such methods is that they do not require the linearization of the NtD map (see, e.g., [22, Prop. 2.1]). This avoids issues associated with local minima as encountered with least-squares methods. However, such techniques are very computationally intensive; each voxel in the imaging domain requires a numerical simulation plus an eigenvalue estimation. Further, the method does not provide information about the contrast between the background and the perturbation.

**1.4. Filtering and image reconstruction.** Although filtering/beamforming appears to be a new concept in the context of low-frequency electromagnetic imaging [12], the idea of using filtering to improve image reconstruction in the context of high-frequency wave-based (e.g., acoustic) imaging has been explored in the past [3, 7, 26, 46, 51].

For instance, Haddadin and Ebbini [26], Tanter et al. [46], Aubry et al. [3], and Vignon et al. [51] have each proposed methods to produce filter/signals such that, when applied at the transducer array, will generate a predetermined pattern (generally a well-localized function) on a focal/control plane. The goal of these techniques is to use a pattern that exhibits better spatio-temporal focusing than traditional techniques (e.g., time reversal) in complex environments such as reflective, reverberating, and absorbing media. The methods are designed for high-frequency, high-bandwidth signals, are all singular value decomposition (SVD) based and produce an “optimal” filter in the least-squares sense. In Tanter et al. [46], the method has been shown to marginally improve focusing experimentally in the limited case of a linear transducer array and linear control plane in a homogeneous medium. In the case of an inhomogeneous medium, however, significant improvements have been shown under various experimental scenarios of practical interest [3]. The main drawback of the latter technique for the treatment of inhomogeneous media is the necessity to know the whole “transfer matrix” (Green’s function). This requires either significant a priori knowledge of the medium, or invasive measurements. Another, less invasive method, presented in Vignon et al. [51] requires only the knowledge of the Green's function between each transducer array element and between the focus point and the transducer array elements in a lossless medium. We note, however, that all the aforementioned methods have a goal of focusing energy at a particular point within an inhomogeneous medium by emitting high-bandwidth signals, and not to locate scatterers within such a medium or to image the medium per se using narrow-bandwidth, low-frequency waves, as intended in this paper.

When it comes to actual imaging, a scheme based on filtering and capable of achieving better cross-range resolution than is possible using traditional techniques (e.g., Kirchhoff migration) in the context of a small active and passive linear transducer arrays is presented by Borcea et al. [7]. The technique is limited to far-field imaging at high frequency in a homogeneous medium. The authors perform a theoretical and numerical study of the problem and show that filtering can improve resolution, but it is highly sensitive to the signal-to-noise ratio (SNR, [7, eq. (24)]. Such sensitivity arises from the use of a least-squares criterion to design the filter and the subsequent ill-conditioning of the reconstruction process (pseudo-inverse of an ill-conditioned matrix). Their approach is conceptually similar to ours in the sense that the goal in designing a filter is to isolate the information in the filtered received signal to small regions of space while negating the effects of perturbations outside these regions as much as possible. One major difference, however, is that Borcea et al. [7] attempt to design a single filter that will improve the refocusing over a large number of locations *all at once*, whereas our method uses *different filters for each location* and then proceeds to a rasterizing step (section 4).

**1.5. Our contributions.** This paper's contributions can be summarized as follows:

- *Low-frequency three-dimensional (3D) electromagnetic imaging based on a novel filtering scheme (section 4)*: we present a new computational 3D imaging framework for complex electromagnetic media capable of achieving significantly better range and cross-range resolution than existing techniques at low frequencies.
- *Fast algorithms (section 3)*: we introduce powerful new fast algorithms for computing the numerical solution of Maxwell's equations in complex anisotropic media. These algorithms go much beyond current techniques, and are key in making this type of imaging possible.
- *Quantification of resolution (section 5)*: we provide a methodology (with numerical examples) to quantify the achievable spatially dependent resolution given a particular imaging scenario.

Our proposed method uses the full system of Maxwell's equations (7) without simplifications.[2] In particular, this implies that the resulting fields carry information about all the properties of the material anisotropic tensors. Our focus in this paper is on imaging conductive structures in an inhomogeneous background, although the principles underlying the method generalize to more complex problems. Our imaging scheme uses a special type of filtering and rasterizing (section 4). At high frequency, the concept is analogous to that of beamforming found in radar [36] and medical imaging [33, 40] applications. We underline, however, that

[2]The only assumption is that of linearity of the material properties; we assume that the electric displacement and magnetic flux are *linearly related* to the electric field and magnetic field, respectively. This is an extremely common assumption.

low-frequency applications are much less analytically tractable than high-frequency techniques given the absence of closed-form analytical formulas, and that our method, given its computational nature, addresses theses issues at low-frequency and is completely novel. Indeed, Chitturi and Nagi [12] describe "low-frequency beamforming" as a promising research direction, given the significant success it has had at high frequency. Even so, no such techniques have been devised up to this point to the authors' knowledge.

With few exceptions [1, 15, 16, 22], all aforementioned references that include numerical results do so in two dimensions. In great part, this is due to the computational difficulties associated with performing large electromagnetic simulations (e.g., [26]). Our fast algorithm overcomes this bottleneck and allows us to study fully 3D problems, and to perform imaging on practical scales.

Finally, despite the vast array of techniques and algorithms for low-frequency imaging (section 1.3), there have been very few quantitative investigations of the achievable resolution.[3] Indeed, to the authors' knowledge, there is only one recent paper that addresses the issue, namely, Harrach and Ullrich [28]. To do so, they use a monotonicity-based technique on a predefined resolution grid. Their method is quite different from the broad-range methodology presented here and significantly more computationally expensive. Furthermore, it has the potential to grossly overestimate the resolution given the need for selecting a resolution grid a priori. Our proposed method is unaffected by these shortcomings.

## 2. Theoretical background.

In this section, we introduce the problem and the notation we shall use throughout this paper. First, we designate the 3D *electric field* and *magnetic field* by $E(x)$ and $H(x)$, $x \in \mathbb{R}^3$. We also denote the spatially dependent *permittivity, conductivity*, and *permeability tensors* by $\epsilon(x)$, $\sigma(x)$, and $\mu(x)$, respectively, and let the constants $\epsilon_0$ and $\mu_0$ be the permittivity and permeability of vacuum.[4] These properties characterize the *medium* through which electromagnetic waves propagate (Maxwell's equations, (7)). We further restrict our attention to *diagonal* tensors; i.e.,

(6)
$$\epsilon(x) = \begin{bmatrix} \epsilon^x(x) & 0 & 0 \\ 0 & \epsilon^y(x) & 0 \\ 0 & 0 & \epsilon^z(x) \end{bmatrix},\ \sigma(x) = \begin{bmatrix} \sigma^x(x) & 0 & 0 \\ 0 & \sigma^y(x) & 0 \\ 0 & 0 & \sigma^z(x) \end{bmatrix},\ \mu(x) = \begin{bmatrix} \mu^x(x) & 0 & 0 \\ 0 & \mu^y(x) & 0 \\ 0 & 0 & \mu^z(x) \end{bmatrix}.$$

The special case where all three diagonal components are equal is referred to as the *isotropic* case. Such restrictions simplify the analysis and the presentation of the results but do not reduce the scope of the technique, which can deal with general two-tensor fields. Finally, $\omega = 2\pi f$ represents the *angular frequency* (Hz) and $\lambda$ is the wavelength (m), which is assumed to be much larger than the imaging region throughout the paper ($\lambda \gg 1$, low frequency). Superscripts of the form $\cdot^x$, $\cdot^y$, $\cdot^z$ will be used to denote the *Cartesian components* of the quantity under consideration. In particular, one should not confound the superscript and the argument in the expressions. For instance, $E^y(x)$ refers to the $y$-component of the electric field evaluated at $x \in \mathbb{R}^3$. The physical model underlying the proposed technique consists of

[3] This is similar to the Rayleigh resolution limit familiar in far-field, high-frequency imaging.
[4] $\epsilon_0 = 8.85418781 \cdot 10^{-12}$F/m. $\mu_0 = 1.25663706144 \cdot 10^{-6}$ H/m.

the time-harmonic (single-frequency) version of Maxwell's equations,

$$\begin{aligned} \nabla \times H(x) - (i\omega\epsilon(x) + \sigma(x))E(x) = J(x), \\ \nabla \times E(x) + i\omega\mu(x)H(x) = M(x), \end{aligned} \tag{7}$$

where it is assumed that there is no free charge density; i.e., $\nabla \cdot J(x) = 0$. Here, $J(x)$ and $M(x)$ are the *electric and magnetic source currents*. This system can be rewritten in operator form (following the notation of Dorn et al. [16]) as

$$\Lambda_M(a,b)\, u(x) = \begin{pmatrix} -b(x) & \nabla\times \\ \nabla\times & a(x) \end{pmatrix} u(x) = q(x), \tag{8}$$

$$\Lambda_M^*(a,b)\, v(x) = \begin{pmatrix} \overline{-b(x)} & \nabla\times \\ \nabla\times & \overline{a(x)} \end{pmatrix} v(x) = q(x), \tag{9}$$

where $a(x) = i\omega\mu(x)$, $b(x) = i\omega\epsilon(x) + \sigma(x)$, and

$$q(x) = \begin{pmatrix} J(x) \\ M(x) \end{pmatrix}.$$

Here, $\bar{\cdot}$ represents the conjugate of a complex number, or the conjugate transpose of a matrix depending on the context. $\Lambda_M(a,b)$ is referred to as the *forward Maxwell operator*, whereas $\Lambda_M^*(a,b)$ is referred to as the *adjoint Maxwell operator*. We shall assume that sources take the form of point magnetic dipoles, i.e.,

$$q_j(x) = \begin{pmatrix} 0 \\ m_j\, \delta(x - x_j) \end{pmatrix}, \tag{10}$$

where the sources are listed through the index $j \in \{1, \ldots, J\}$, $\{m_j\}$ are their respective dipole moments, and $\{x_j\}$ represent their locations in $\mathbb{R}^3$. Note that this assumption is by no means necessary; most sources can be treated numerically using, for instance, properly discretized single- and/or double-layer (vector) potentials, corresponding to sums of dipoles (see, e.g., [13, section 2.2]). With this notation, the field generated by $q_j(x)$ is denoted $u_j(x)$, and the *measured data*, denoted $d_j$, correspond to a vector of size $6 \cdot N$. If each receiver location is identified by the index $n \in \{1, \ldots, N\}$, the entries of $d_j$ correspond to the field $u_j(x)$ at location $x_n$, i.e.,[5]

$$d_j = [u_j(x_1);\, u_j(x_2);\, \ldots\, u_j(x_N)]\,, \tag{11}$$

where ";" denotes vertical concatenation. Under the appropriate circumstances,[6] the Maxwell operators map a source distribution $q(x)$ to electromagnetic fields $u(x)$, $v(x)$ through the unique solution of their respective PDE systems (8)–(9). In other words, $\Lambda_M(a,b)^{-1}\, q(x)$ and $[\Lambda_M^*(a,b)]^{-1}\, q(x)$ are well-defined. Under this setup, the goal of our imaging scheme can

[5] It is assumed that all six components of the field can be measured and are available for imaging purposes (6-axis receivers).

[6] These circumstances are sufficient regularity of the right-hand side and of the coefficients $a(x)$, $b(x)$, together with the Sommerfeld radiation conditions at infinity.

be stated as follows: to determine the medium properties $a(x)$ and $b(x)$ from electrical and magnetic fields measurements $\{d_j\}$ induced by a set of known sources $\{q_j(x)\}$ located outside of the imaging region. To achieve this goal, our proposed technique relies on three algorithmic components:

1. *Adjoint field method* (section 2.1) for the inversion of the data and for gaining theoretical insights into the inverse problem.
2. *Low-complexity algorithms* ($O(N\log(N))$; section 3) for the simulation of electromagnetic waves through inhomogeneous background media.
3. *Filtering and rastering imaging scheme* (section 4) to overcome the shortcomings of the standard adjoint field method and to improve and quantify the resolution.

We note once again that the speed of the aforementioned fast algorithm is critical to our scheme and constitutes its backbone. Indeed, as mentioned in section 3, fast algorithms allow us to treat large computational problems at practical scales. In the sections that follow, we elaborate on each component.

**2.1. Adjoint method framework and sensitivity function decomposition.** In this section, we introduce the adjoint field method for solving the inverse problem described earlier in section 2 (see also [16]). The starting point of the scheme is the *residual operator*,

$$R(a,b) = \begin{bmatrix} d_1 \\ d_2 \\ \cdots \\ d_J \end{bmatrix} - \begin{bmatrix} \mu_1 \\ \mu_2 \\ \cdots \\ \mu_J \end{bmatrix} = d - \mu, \tag{12}$$

where $d_j$ are the physically measured data generated through the $j$th source $q_j(x)$, and $\mu_j = \Lambda_M^{-1}(a,b)\,q_j(x)$ corresponds to the numerically simulated measurements obtained using medium property estimates $a(x)$ and $b(x)$. Under this setup, the adjoint field method can be described as an output least-squares method (section 1.1) where the goal is to recover some distributions $a^*(x)$ and $b^*(x)$ that minimize the squared norm of the residual, i.e.,

$$(a^*(x),\, b^*(x)) = \mathrm{argmin}_{a(x),b(x)}\, ||R(a,b)||^2 \tag{13}$$

over all admissible distributions $a(x)$ and $b(x)$, where $||\cdot||$ represents the $L^2(\mathbb{R}^3)$-norm. To do so, one makes use of three ingredients: (1) a linearization of $R(a,b)$ about the current medium estimate (Fréchet derivative), (2) a least-squares-based Newton–Raphson iteration, and most importantly (3) a computationally efficient approximation scheme for solving the linear system arising at each Newton–Raphson step. We begin with a description of the linearization. For this purpose, details regarding the explicit form of the linearized residual operator and its adjoint can be found in Theorem 1 below.

Theorem 1 ([16, Theorems 3.1–4.1], linearized operators, multiple sources). *For each source $q_j$, $j = 1,\ldots,J$, let $[\mu_j]_n$ be the simulated data vector induced and measured at $x_n$ for $n = 1,\ldots,N$ with medium property estimates $a(x)$ and $b(x)$. Further, let $E_j(x)$, $H_j(x)$, $\mathcal{E}_j(x)$, and*

*$\mathcal{H}_j(x)$ be the solutions to the following problems:*

$$\Lambda_M(a,b)\begin{pmatrix}E_j(x)\\H_j(x)\end{pmatrix}=q_j(x), \tag{14}$$

$$\Lambda_M^*(a,b)\begin{pmatrix}\mathcal{E}_j(x)\\\mathcal{H}_j(x)\end{pmatrix}=\sum_{n=1}^{N}[d_j]_n\,\delta(x-x_n). \tag{15}$$

*Then the linearized residual operator $R'[a,b]$ and its adjoint $R'[a,b]^*$ take the form,*

$$\left[R'[a,b]\begin{pmatrix}\delta b(x)\\\delta a(x)\end{pmatrix}\right]_j=\Lambda_M^{-1}(a,b)\begin{pmatrix}\delta b(x)\,E_j(x)\\-\delta a(x)\,H_j(x)\end{pmatrix}, \tag{16}$$

$$R'[a,b]^*\,d=\sum_j\begin{pmatrix}\operatorname{diag}\left(\bar{E}_j^x(x)\,\mathcal{E}_j^x(x),\ \bar{E}_j^y(x)\,\mathcal{E}_j^y(x),\ \bar{E}_j^z(x)\,\mathcal{E}_j^z(x)\right)\\-\operatorname{diag}\left(\bar{H}_j^x(x)\,\mathcal{H}_j^x(x),\ \bar{H}_j^y(x)\,\mathcal{H}_j^y(x),\ \bar{H}_j^z(x)\,\mathcal{H}_j^z(x)\right)\end{pmatrix}, \tag{17}$$

*where $\delta a(x)$ and $\delta b(x)$ are first-order perturbations about the property fields $a(x)$ and $b(x)$, i.e.,*

$$R(a+\delta a,b+\delta b)=R(a,b)+R'[a,b](\delta a(x),\delta b(x))+O\left(||\delta a(x)||^2+||\delta b(x)||^2\right). \tag{18}$$

The proof of this theorem is a straightforward generalization of Theorems 3.1 and 4.1 of [16], to which we refer the reader for further details. The Newton–Raphson step [39] is obtained by minimizing the linearized residual in the least-squares sense, leading to *updates* of the form

$$\begin{pmatrix}\delta b(x)\\\delta a(x)\end{pmatrix}=-R'[a,b]^*\ \left(R'[a,b]\,R'[a,b]^*\right)^{-1}\ R(a,b)\approx-R'[a,b]^*\ R(a,b). \tag{19}$$

From a computational standpoint, the crux of the adjoint field scheme in [16] lies in the approximation

$$\left(R_j'[a,b]\,R_j'[a,b]^*\right)^{-1}=c\,I \tag{20}$$

for some constant $c>0$, together with a careful selection of the sampling configuration and a filtering (nulling) of the resulting update in the vicinity of sources/receivers. This simplified form leads to major advantages in that the updates can now be computed rapidly through the solution of a *single* forward Maxwell equation and adjoint problem, without proceeding to an expensive matrix inversion. However, the quality of this approximation depends on many parameters including the imaging configuration and the medium properties. In this sense, it does not always provide satisfying results (see section 5.1), and further refinements are necessary to overcome these shortcomings. Such refinements are at the core of our approach and are presented in section 4. A discussion and numerical results are also presented in section 5.

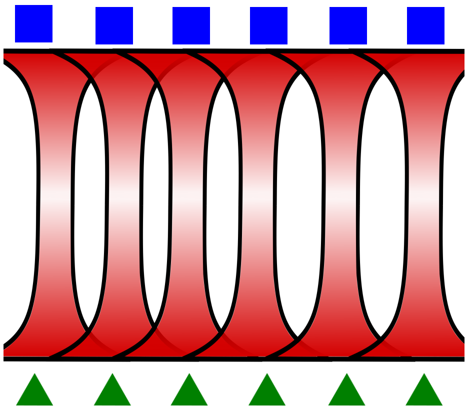

**Figure 1.** *Conceptual schematic of low-frequency sensitivity functions between combinations of sources (green triangles) and receivers (blue squares) in a homogeneous medium (not all receiver/source pairs are represented). For a fixed source/receiver pair, the sensitivity is generally concentrated on the geodesic linking both, and is largest in magnitude close to the source or receiver (intensity in red). Shapes are not to scale and only show the typical characteristics of sensitivity functions (poor localization, smoothness, and complex behavior).*

**2.2. Sensitivity function decomposition.** Another important property of the adjoint field method is the availability of a decomposition for the linearized residual operator and its adjoint in terms of *sensitivity functions*. From an intuitive standpoint, sensitivity functions can be described as follows: a small perturbation of the medium properties at location $x$ leads to a change in the data proportional to the sensitivity function at that particular location. For instance, let the function $\phi(x) : \mathbb{R}^3 \to \mathbb{R}^3$ correspond to the sensitivity function associated with a fixed source and receiver, and suppose it is sensitive to perturbations in the $q$th component of $b(x)$, i.e., in $b^q(x)$. Then, a "small" perturbation $\Delta \cdot \delta(x - x_0)$ of $b^q(x)$ at $x_0$ will lead to a change in the measured data at the receiver of the form: $\Delta\, \phi(x_0)$. We underline a few common characteristics of sensitivity functions at low frequency (some of these features are highlighted schematically in Figure 1. See also Figure 2):

1. *Poor localization*: the sensitivity functions are supported over all of $\mathbb{R}^3$, with larger values close to the geodesic between the source and receiver location and largest values near the source and receiver.
2. *Smooth/nonoscillatory*: the sensitivity functions exhibit little variations, except close to the sources and receivers.
3. *Complex behavior*: the sensitivity functions are complex, vector valued, and exhibit a nontrivial behavior as a function of the source orientation, relative source/receiver locations, and background properties.

These characteristics have far-reaching consequences from an imaging perspective. For instance, poor localization and smoothness imply that different perturbations in the properties may lead to very similar perturbations in the data, leading to an *ill-conditioned* problem. Similarly, the complex behavior implies that it is very difficult to resort to theoretical techniques to derive efficient imaging schemes, and that efficient computational methods must be used. An actual example of a sensitivity function is shown in Figure 2 for a homogeneous background.

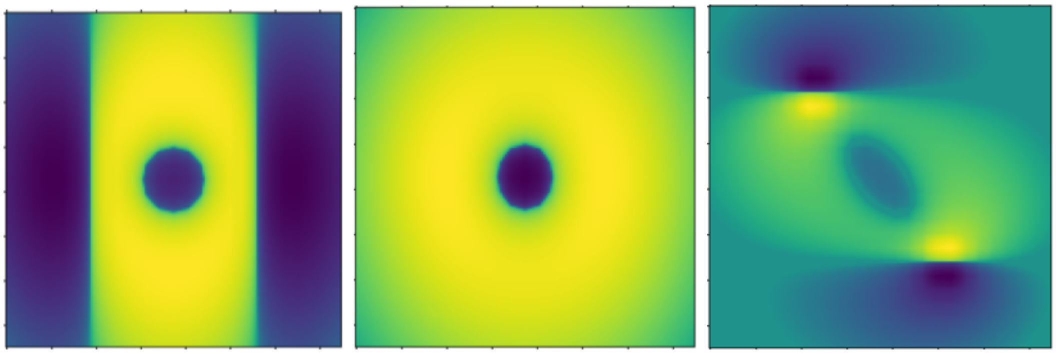

**Figure 2.** *Real part of sensitivity function of the $x$-component of the electric field to perturbations $\delta b^x(x)$. The function plotted is* $\mathrm{sign}(\Re(\phi^{(x,x)}(E,b;\,x)))\,(60+10\,\log(\frac{|\Re(\phi^{(x,x)}(E,b;\,x))|}{\max_x \Re(\phi^{(x,x)}(E,b;\,x))}))$. *The background is homogeneous with a $z$-dipole source at $(0,0,107)\,m$, a $z$-component receiver at $(0,0,42)$ $m$, and $\omega = 30$ kHz ($\lambda \approx 10$ km). From left to right: xy-plane, xz-plane, and yz-plane. Note the presence of typical sensitivity functions: poor localization, smoothness, and complex behavior. In practice, there are a total of six* (6) *sensitivity functions per scalar medium property and source/receiver pair, which can all be leveraged for imaging purposes.*

The demonstration of the existence of the sensitivity function decomposition as well as an explicit representation of the sensitivity functions themselves can be found in Dorn et al. [16, Theorems 5.1 and 5.2]. The results are summarized in Theorem 2 below.

Theorem 2 ([16, Theorem 5.1], Sensitivity function decomposition). *Let $x_j$ and $x_n$ be a fixed source and receiver location, respectively, $m_{j,E}$, $m_{j,H}$ be the source electric and magnetic dipole moments, and let $a(x)$ and $b(x)$ be the medium properties. Then, for each perturbation type $c \in \{a, b\}$, perturbation direction $q \in \{x, y, z\}$, measurement field $K \in \{E, H\}$, and measurement component $p \in \{x, y, z\}$ there exist functions $\phi^{p,q}_{j,n}(K, c; y)$ called* sensitivity functions *such that the linearized residual operator* (16)*) and the linearized residual adjoint operator* (17) *can be written as*

$$\left[R'[a, b]\,\delta b(x)\right]_n = \sum_{p\in\{x,y,z\}} \left( \sum_{q\in\{x,y,z\}} \int \delta c^q(y)\,\phi^{p,q}_{j,n}(y)\,\mathrm{d}y \right) e_p, \tag{21}$$

$$\left(R'[a, b]^*\,d_j\right)\,(x) = \sum_{n=1}^{N} \sum_{p,q\in\{x,y,z\}} d^q_{j,n}\,\overline{\phi^{p,q}_{j,n}(x)}. \tag{22}$$

*Further, the sensitivity functions of the measured field to perturbations in $a(x)$ and $b(x)$, respectively, take the explicit form*

$$\phi^{p,q}_{j,n}(K, a;\, y) = -H^q_j(y)\,\mathcal{H}^q_j(y), \tag{23}$$

$$\phi^{p,q}_{j,n}(K, b;\, y) = E^q_j(y)\,\mathcal{E}^q_j(y), \tag{24}$$

*where $E_j^q(y)$, $H_j^q(y)$ and $\mathcal{E}_j^q(y)$, $\mathcal{H}_j^q(y)$ are the solutions of (14) and (15) with right-hand sides,*

$$q(x) = \begin{pmatrix} m_{j,E} \\ m_{j,H} \end{pmatrix} \delta(x - x_j), \tag{25}$$

$$d(x) = \begin{pmatrix} \delta_{K,E}\, e_p \\ \delta_{K,H}\, e_p \end{pmatrix} \delta(x - x_n), \tag{26}$$

*where $\{e_p\}_{p\in\{x,y,z\}}$ is the canonical basis for $\mathbb{R}^3$.*

The notation of Theorem 2 should be understood as follows: given a fixed source with index $j$ and a fixed receiver located at $x_n$, $\phi_{j,n}^{p,q}(K, b; y)$ represents the size of the change of the $p$th component of the $K$-field measured at the receiver due to a small perturbation of the property distribution $b(y)$ in the $q$-direction.

The decomposition introduced in Theorem 2 forms the backbone of our imaging routine; together with our fast algorithm (section 3), the explicit form of the decomposition allows us to numerically compute powerful “data filters” that can *isolate the effect of perturbations within small regions of space* (nullifying effects outside such regions). In turn, this allows us to generate 3D images. This is described in detail in section 4.

**3. Fast ($O(N\log(N))$) Maxwell's equations solver.** Here, we provide an overview of the algorithm used for simulating the propagation of electromagnetic signals in 3D inhomogeneous media (8)–(9) and for efficiently computing filters in section 4. We underline that this algorithm is absolutely key to the practical implementation of our proposed filtering scheme, as it would otherwise be computationally prohibitive using existing technology. We also refer the reader to [48] for a detailed description. Now, consider

$$\overleftrightarrow{G}(x, y) = \overleftrightarrow{G}(x - y) = \overleftrightarrow{I}\, G(x - y) + \frac{1}{k_0^2} \nabla\nabla G(x - y), \tag{27}$$

where $\overleftrightarrow{I}$ is the $3 \times 3$ identity matrix and $k_0$ is the wavenumber. $G(x) = \frac{e^{ik_0|x|}}{4\pi|x|}$ is generally referred to as the *Helmholtz Green's function*, whereas $\overleftrightarrow{G}(x, y)$ is referred to as the *dyadic Green's function.*[7] Then, it can be shown (see Appendix A) that,

$$\begin{bmatrix} E(x) \\ H(x) \end{bmatrix} = \begin{bmatrix} E_0(x) \\ H_0(x) \end{bmatrix} + \begin{bmatrix} A_{11} & A_{12} \\ A_{21} & A_{22} \end{bmatrix} \begin{bmatrix} E(x) \\ H(x) \end{bmatrix},$$

where

(28)
$$A_{11}(Q(x)) = -i\omega\mu_0 \int \overleftrightarrow{G}(x, y)\, \tilde{b}(y)\, Q(y)\mathrm{d}y, \quad A_{12}(Q(x)) = \int \nabla \times \overleftrightarrow{G}(x, y)\, (-\tilde{a}(y))\, Q(y)\mathrm{d}y,$$

(29)
$$A_{21}(Q(x)) = \int \nabla \times \overleftrightarrow{G}(x, y)\, \tilde{b}(y)\, Q(y)\mathrm{d}y, \qquad A_{22}(Q(x)) = i\omega\epsilon_0 \int \overleftrightarrow{G}(x, y)\, (-\tilde{a}(y))\, Q(y)\mathrm{d}y,$$

[7] $G(x)$ is the fundamental solution to the scalar, homogeneous, time-harmonic wave equation: $\left(\nabla^2 + k_0\right) G(x) = -\delta(x)$ in $\mathbb{R}^3$, where $\nabla^2$ is the Laplacian and $\delta(\cdot)$ is a Dirac delta at the origin. Similarly, $\overleftrightarrow{G}(x)$ is the fundamental solution to the time-harmonic vector wave equation: $(\nabla\times\nabla\times - \nabla\nabla\cdot)u(x) + k_0^2 u(x) = -\delta(x)\,\overleftrightarrow{I}$ in $\mathbb{R}^3$.

which, upon appropriate discretization of the integrals, leads to

$$\begin{bmatrix} E(x) \\ H(x) \end{bmatrix} = (I - A)^{-1} \begin{bmatrix} E_0(x) \\ H_0(x) \end{bmatrix}.$$

Our solver computes this solution using an iterative linear solver (LGMRES [4]). This requires applications of the dense matrix $(I - A)$ to various vectors, an $O(N^2)$ operation if performed naïvely, and thus too expensive for problems of practical scales.

To improve performance, we apply $A$ rapidly using an algorithm that consists of a generalization of the FFT-based algorithm introduced by Vico, Greengard, and Ferrando [50] to electromagnetism [48]. By leveraging the speed of the FFT, this scheme leads to a fast $(O(N \log(N))$ algorithm for the application of the matrix $A$. We also refer the reader to Vico, Greengard, and Ferrando [50] and Tong et al. [48] for a more detailed discussion on the discretization of the integral, the choice of $N$, the appropriate scaling involved, and potential optimizations. Pseudocode can be found in [48]. We have implemented a parallel version of the algorithm in the C programming language using OpenMP, and have used it to produce the numerical results found in section 5. We refer to Tong et al. [48] for a more in-depth study of performance.

## 4. Filtering and imaging.

As discussed in section 5.1, the standard adjoint field method presented in section 2.1 suffers from many drawbacks at low frequency including a lack of range resolution and poor cross-range resolution. To overcome these shortcomings, we introduce in this section a new imaging scheme. The most important characteristic of our proposed method lies in replacing the matrix $(R'[a, b]\, R'[a, b]^*)^{-1}$ in the Newton–Raphson step (19)) with a filtering matrix $F$ designed to tailor the sensitivity to regions around specific (steering) points. Intuitively, the scheme can be described as follows: first, we choose a set $\{x_l\}$ of *steering points* (Figure 3) where we want to concentrate/focus the sensitivity, i.e., perturbations in a 3D region surrounding a steering point should have a large effect on the filtered data, whereas perturbations far from the latter should have almost no effect. Then, we proceed to a rasterizing process through each steering point. Points corresponding to the location of a perturbation will lead to a large contribution (weight) after filtering, and vice versa. This information is used to generate an image.

For all that follows, we consider isotropic perturbations in $b(x)$ only ($\delta b^x(x) = \delta b^y(x) = \delta b^z(x)$, $\delta a(x) \equiv 0$). This has the advantage of significantly simplifying the notation without affecting the generality of the method. A consequence of isotropy is that the quantities found in Theorems 1–2 become

$$\phi^{p}_{j,n}(K;\, y) = \sum_{q \in \{x,y,z\}} \phi^{p;q}_{j,n}(K, b;\, y) \tag{30}$$

for the sensitivity functions, and

$$\begin{aligned} &R'[a, b]^* d \\ &= \sum_{j=1}^{J} \begin{pmatrix} \mathrm{diag}(\sum_{q\in\{x,y,z\}} \overline{E^q_j(x)}\mathcal{E}^q_j(x), \sum_{q\in\{x,y,z\}} \overline{E^q_j(x)}\mathcal{E}^q_j(x), \sum_{q\in\{x,y,z\}} \overline{E^q_j(x)}\mathcal{E}^q_j(x)) \\ -\mathrm{diag}(\sum_{q\in\{x,y,z\}} \overline{H^q_j(x)}\mathcal{H}^q_j(x), \sum_{q\in\{x,y,z\}} \overline{H^q_j(x)}\mathcal{H}^q_j(x), \sum_{q\in\{x,y,z\}} \overline{H^q_j(x)}\mathcal{H}^q_j(x)) \end{pmatrix} \end{aligned} \tag{31}$$

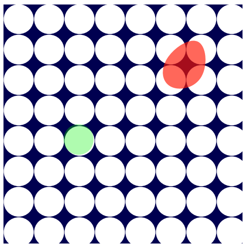

(a) The induced sensitivity region associated with the current steering point (green) does not coincide with the location of a perturbation/scatterer (red). The steering point has no effect on the image (zero weight).

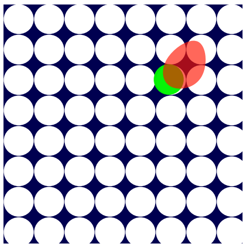

(b) The induced sensitivity region associated with the current steering point (green) coincides with the location of a perturbation/scatterer (red). The steering point will contribute to the image (nonzero weight).

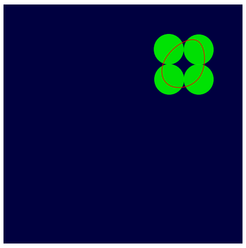

(c) The resulting image corresponds to a weighted sum of induced sensitivity functions that approximate the original perturbation.

**Figure 3.** *Schematic of imaging scheme through steering, filtering, and rastering. White circles correspond to steering points ($\{x_l\}$). Green circles represent current steering point (region of high sensitivity induced through filtering) and the red region represents the perturbation.*

for the linear residual residual adjoint operator. To design the filters, we rely heavily on the sensitivity function decomposition of Theorem 2 and proceed as follows: given a fixed steering point $x_l$ and an associated set of *filter coefficients* $\{f_l(j,n,p,K)\}$, define an *induced sensitivity function* through

$$\eta_l(y) := \sum_{j,n,p,K} f_l(j,n,p,K)\overline{\phi^p_{j,n}(K;y)}. \tag{32}$$

With this definition and Theorem 2, the filtering process can be expressed as

$$\sum_{j,n,p,K} \overline{f_l(j,n,p,K)}\, d^p_{j,n,K} = \int \delta b(y) \left( \sum_{j,n,p} \overline{f_l(j,n,p,K)}\, \phi^p_{j,n}(K;y) \right) \mathrm{d}y \tag{33}$$

$$= \int \delta b(y)\, \overline{\eta_l(y)}\, \mathrm{d}y, \tag{34}$$

which is a projection of the perturbation $\delta b(x)$ onto the induced sensitivity function $\eta_l(y)$. In this sense, our goal in designing a filter is to *maximize the energy of $\eta_l(y)$ in the vicinity of $x_l$ and minimize it away from $x_l$.*

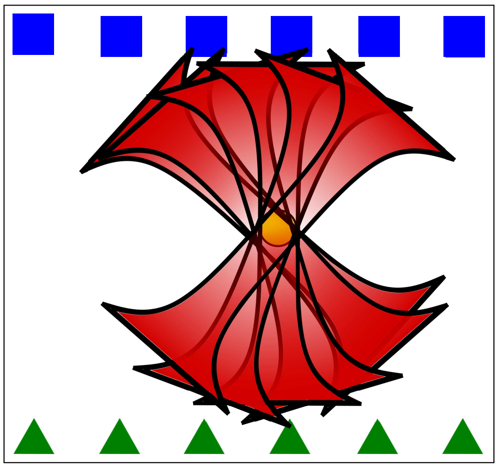

(a) Imaging using the standard adjoint field method (section 2.1). The image is a trivial linear combinations of the sensitivity functions corresponding to the backprojection of the data ((22), Theorem 2). Energy is located over a hyperbolic region, providing poor range resolution.

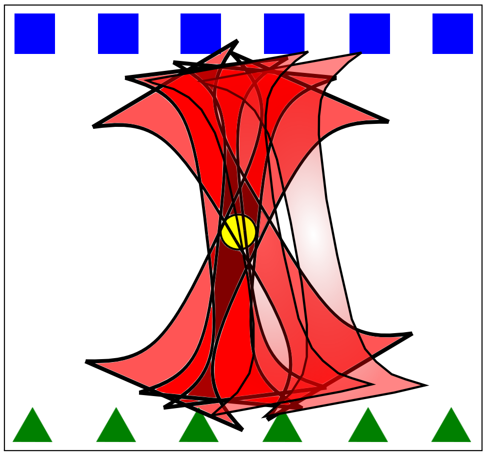

(b) Imaging using our proposed method. The image is a *weighted* linear combinations of overlapping induced sensitivity functions, and corresponds to the backprojection of the *filtered data* (34). Energy is highest in a small 3D region around the scatterer, providing good range and cross-range resolution.

**Figure 4.** *Conceptual schematics of imaging with sensitivity functions. Sources are represented by green triangles and receivers are represented by blue rectangles. The perturbation is located at the yellow circle. Left: standard adjoint field method. Right: our filtering scheme. Note that in each scenario there are sensitivity functions between every source and every receiver. Each figure depicts distinct subsets of such functions.*

The filtering process itself is depicted schematically in Figure 4 for the case of linear and parallel receiver/source arrays with backward illumination and a steering point located at the center; the left of Figure 4(a) shows the result of the standard adjoint field method (section 2.1) that corresponds to setting $f(j, n, p, K) = 1$. In this case, the image has energy concentrated in a "hyperbolic" region with cross section smallest in the plane of the scatterer. This implies that cross-range resolution is achievable with such a scheme. However, this type of image offers no range resolution since the intensity is approximately the same along the whole range direction (and sometimes even larger near the source/receivers, which is completely erroneous. See Figure 5). In contrast, Figure 4(b) shows the effect of appropriately weighting the sensitivity functions prior to forming the image (our data filtering scheme). In this case, the image produced corresponds to the induced sensitivity function $\eta_l(y)$ associated with this steering point. By design, the induced sensitivity function possesses most energy in a 3D region localized about the point of interest (overlapping weighted sensitivity functions, darker red region in figure) which offers both cross-range and range resolution. The creation of the filters is followed by a *rasterizing process*, by which we focus the sensitivity on one steering point at a time to identify locations and size of perturbations. This is depicted pictorially in Figure 3. More precisely, given some data vector $d$, we apply the filter $f_l$ to compute

$$d_l = f_l f_l^* \, d \tag{35}$$

for each steering point $x_l$. Then, we backpropagate each of the filtered data and sum the

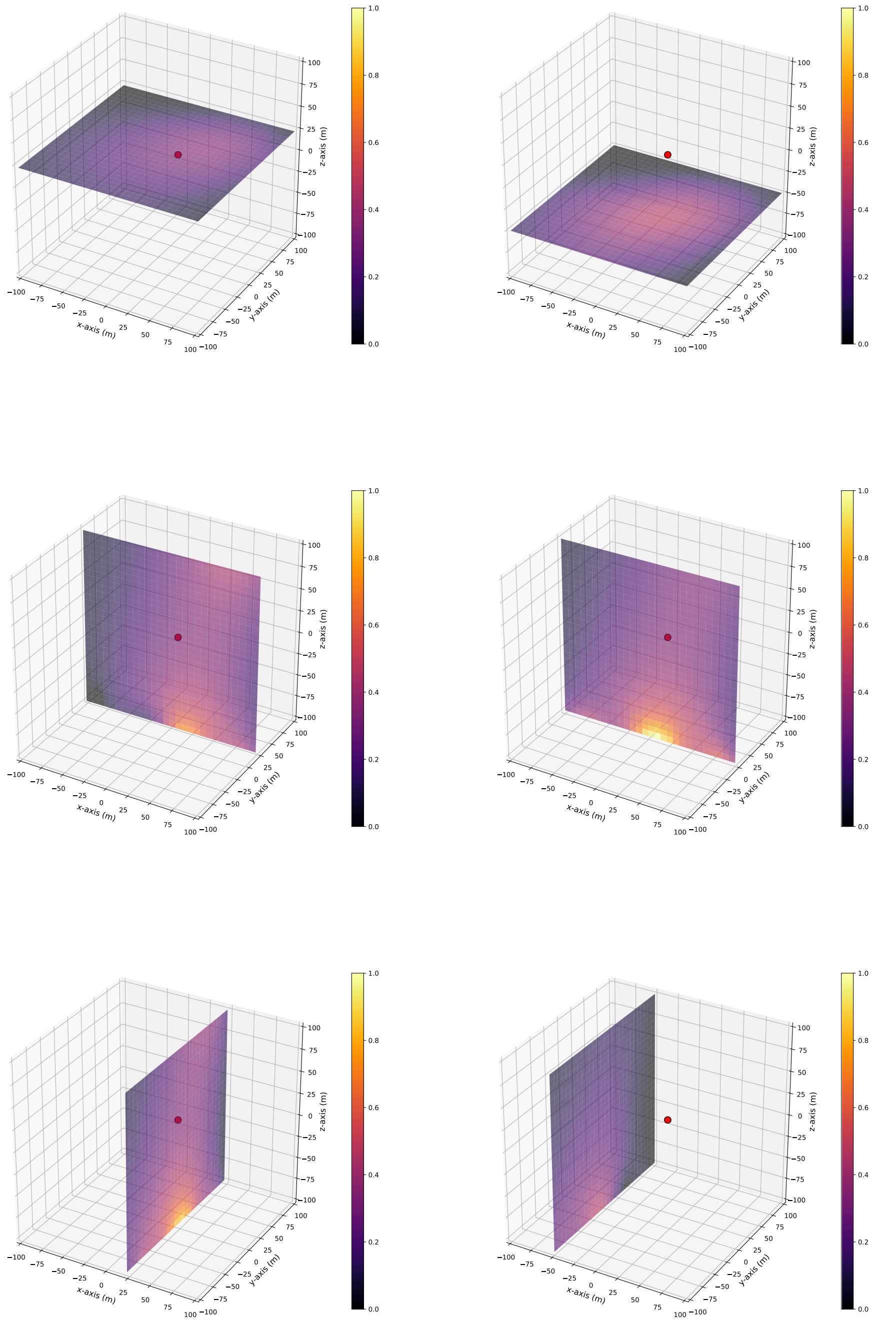


**Figure 5.** *Cross-sectional (two-dimensional (2D)) views of the (3D) image reconstructed using output least squares with Tikhonov regularization. Scatterer located at* $(22, 0, 22)\,m$ *between* $3 \times 3$ *source and receiver parallel arrays at* $z = \pm 150$ *m. From left to right, top to bottom: xy-plane,* $z = 22$ *m; xy-plane,* $z = -50$ *m; xz-plane,* $y = 22$ *m; xz-plane,* $y = 0$ *m; yz-plane,* $x = 22$ *m; yz-plane,* $x = -50$ *m. Cross-range resolution is poor. There is no range resolution.*

results to produce the image.[8] In the case of an isotropic medium, we obtain

$$\mathcal{I} := \sum_l R'[a,b]^* \, d_l = R'[a,b]^* \left( \sum_l f_l f_l^* \right) d = R'[a,b]^* \, F \, d, \tag{36}$$

where $R'[a,b]^*$ is the linearized residual adjoint of (17), and $F := \sum_l f_l f_l^*$ is the replacement of $(R'[a,b]\, R'[a,b]^*)^{-1}$ in (19). $F$ can be interpreted as an operator that projects the perturbation onto the induced sensitivity functions for which energy is more closely focused near the perturbation.[9] This is summarized in Algorithm 1. Putting everything together, we find that the image $\mathcal{I}$ takes the form

(37)
$$\mathcal{I} = \sum_l \left[ \left( \int \delta b(y)\, \eta_l(y)\, \mathrm{d}y \right) \left( \sum_{j,n,p,K} \overline{f_l(j,n,p,K)}\, \phi^p_{j,n}(x) \right) \right] = \sum_l \left[ \left( \int \delta b(y)\, \overline{\eta_l(y)}\, \mathrm{d}y \right) \eta_l(x) \right].$$

This expression shows that the image produced by our scheme is in fact a backprojection of the perturbation on a family of *induced* sensitivity functions. This use of induced sensitivity functions through the design of appropriate filters gives us more flexibility throughout the imaging process and ultimately leads to higher resolution (section 5). The design and computation of such filters is discussed next.

**Algorithm 1** 3D sensitivity-function-based imaging algorithm (single step).

Input: $d$ (data), $a(x), b(x)$ (medium estimates), $\{f_l\}_{l=1}^L$ (filters associated w/ steering points $\{x_l\}_{l=1}^L$)
Let: $\tilde{d} = 0$
**for** $l \in \{1, 2, \ldots, L\}$ **do**
  $\tilde{d} \leftarrow \tilde{d} + f_l f_l^* \, d$
**end for**
Compute: $\mathcal{I} = \begin{pmatrix} \delta a(x) \\ \delta b(x) \end{pmatrix} = R'[a,b]^* \, \tilde{d}$ , (17)
Output: $\mathcal{I}$

The procedure for creating a filter can be described as follows: first, we consider a set $G = \{x_\alpha\}_{\alpha=1}^{N_G}$ of "good points" as well as a set $B = \{x_\beta\}_{\beta=1}^{N_B}$ of "bad points." $G$ generally contains a single point corresponding to the current steering point where we want the highest sensitivity, whereas $B$ represents the complement of $G$ in the imaging window where we want to "nullify" sensitivity. For instance, in Figure 3(a)–(b) the set $G$ consists of the green steering

[8] The summation step corresponds to a (virtual) form of a rasterizing process for induced sensitivity functions with disjoint supports.

[9] This idea generalizes to any form of sensor measurements when a notion of sensitivity function is present. See, for example, Mountcastle, Goodman, and Morgan [36] for an application referred to as *beamforming* and applied to radar problems.

point only, whereas $B$ contains all the remaining (white) points. The goal then is to choose filter coefficients $\{f_l\}$ that maximize the ratio

$$\frac{\sum_{x_\alpha \in G} |\eta_l(x_\alpha)|^2}{\sum_{x_\beta \in B} |\eta_l(x_\beta)|^2} = \frac{\sum_{x_\alpha \in G} \left|\sum_{j,n,p,K} \overline{f_l(j,n,p,K)}\, \phi^p_{j,n}(x_\alpha)\right|^2}{\sum_{x_\beta \in B} \left|\sum_{j,n,p,K} \overline{f_l(j,n,p,K)}\, \phi^p_{j,n}(x_\beta)\right|^2}. \tag{38}$$

That is, we seek to maximize the power of the induced sensitivity function over the set $G$ while minimizing it over $B$. Equation (38) can be put in matrix form:

$$\text{argmax}_{\{f_l\}} \frac{||\mathcal{A}\, f_l||^2}{||\mathcal{B}\, f_l||^2}, \tag{39}$$

where the $(6N_G \times 6JN)$ matrix $\mathcal{A}$ and the $(6N_B \times 6JN)$ matrix $\mathcal{B}$ take the form

(40)
$$\mathcal{A} = \begin{bmatrix} \phi^{(x,x)}_{(1,1)}(E; x^{(G)}_1) & \phi^{(x,x)}_{(1,1)}(H; x^{(G)}_1) & \phi^{(x,y)}_{(1,1)}(E; x^{(G)}_1) & \cdots & \phi^{(x,x)}_{(1,2)}(H; x^{(G)}_1) & \cdots & \phi^{(x,z)}_{(J,N)}(H; x^{(G)}_1) \\ \phi^{(y,x)}_{(1,1)}(E; x^{(G)}_1) & \phi^{(y,x)}_{(1,1)}(H; x^{(G)}_1) & \phi^{(y,y)}_{(1,1)}(E; x^{(G)}_1) & \cdots & \phi^{(y,x)}_{(1,2)}(H; x^{(G)}_1) & \cdots & \phi^{(y,z)}_{(J,N)}(H; x^{(G)}_1) \\ \cdots & \cdots & \cdots & \ddots & \cdots & \ddots & \cdots \\ \phi^{(z,x)}_{(1,1)}(E; x^{(G)}_{N_G}) & \phi^{(z,x)}_{(1,1)}(H; x^{(G)}_{N_G}) & \phi^{(z,y)}_{(1,1)}(E; x^{(G)}_{N_G}) & \cdots & \phi^{(z,x)}_{(1,2)}(H; x^{(G)}_{N_G}) & \cdots & \phi^{(z,z)}_{(J,N)}(H; x^{(G)}_{N_G}) \end{bmatrix},$$

(41)
$$\mathcal{B} = \begin{bmatrix} \phi^{(x,x)}_{(1,1)}(E; x^{(B)}_1) & \phi^{(x,x)}_{(1,1)}(H; x^{(B)}_1) & \phi^{(x,y)}_{(1,1)}(E; x^{(B)}_1) & \cdots & \phi^{(x,x)}_{(1,2)}(H; x^{(B)}_1) & \cdots & \phi^{(x,z)}_{(J,N)}(H; x^{(B)}_1) \\ \phi^{(y,x)}_{(1,1)}(E; x^{(B)}_1) & \phi^{(y,x)}_{(1,1)}(H; x^{(B)}_1) & \phi^{(y,y)}_{(1,1)}(E; x^{(B)}_1) & \cdots & \phi^{(y,x)}_{(1,2)}(H; x^{(B)}_1) & \cdots & \phi^{(y,z)}_{(J,N)}(H; x^{(B)}_1) \\ \cdots & \cdots & \cdots & \ddots & \cdots & \ddots & \cdots \\ \phi^{(z,x)}_{(1,1)}(E; x^{(B)}_{N_B}) & \phi^{(z,x)}_{(1,1)}(H; x^{(B)}_{N_B}) & \phi^{(z,y)}_{(1,1)}(E; x^{(B)}_{N_B}) & \cdots & \phi^{(z,x)}_{(1,2)}(H; x^{(B)}_{N_B}) & \cdots & \phi^{(z,z)}_{(J,N)}(H; x^{(B)}_{N_B}) \end{bmatrix}.$$

We recall that $J$ is the total number of sources and $N$ is the total number of receivers. Equation (39) corresponds to a *generalized Rayleigh ratio*, and can be maximized by solving an appropriate (generalized) eigenvalue problem. The procedure, which we now summarize, is also presented in Algorithm 2. Consider the SVD of $\mathcal{B}$: $\mathcal{B} = U_{\mathcal{B}}\Sigma_{\mathcal{B}}V^*_{\mathcal{B}}$. With this quantity, the generalized Rayleigh ratio takes the form

$$\frac{f^*\mathcal{A}^*\mathcal{A}f}{f^*\mathcal{B}^*\mathcal{B}f} = \frac{f^*\mathcal{A}^*\mathcal{A}f}{f^*V_{\mathcal{B}}\Sigma^2_{\mathcal{B}}V^*_{\mathcal{B}}f}. \tag{42}$$

Proceeding to the change of variable, $f = V_{\mathcal{B}}\Sigma^{-1}_{\mathcal{B}}f$, we obtain

$$\frac{f^*\Sigma^{-1}_{\mathcal{B}}V^*_{\mathcal{B}}\mathcal{A}^*\mathcal{A}V_{\mathcal{B}}\Sigma^{-1}_{\mathcal{B}}f}{f^*f} = \frac{||\mathcal{A}V_{\mathcal{B}}\Sigma^{-1}_{\mathcal{B}}f||^2}{||f||^2}, \tag{43}$$

which is a standard Rayleigh ratio, the maximum of which is reached when $f$ corresponds to the right singular vector $\xi$ of $\mathcal{A}V_{\mathcal{B}}\Sigma^{-1}_{\mathcal{B}}$ associated with the largest singular value. Once computed, we normalize the resulting quantity to get

$$f = \frac{V_{\mathcal{B}}\Sigma^{-1}_{\mathcal{B}}\,\xi}{\left|\left|R'[a,b]^*\, V_{\mathcal{B}}\Sigma^{-1}_{\mathcal{B}}\,\xi\right|\right|_\infty}. \tag{44}$$

This choice of normalization is based on the the explicit form of the image formation expression found in (36). Indeed, if $\delta b(y) = \operatorname{diag}(\delta b_0, \delta b_0, \delta b_0)\, \delta(y - y_0)$ is an isotropic point scatterer, then

$$
\begin{aligned}
\mathcal{I} &= \left[R'[a,b]^*(F\, d)\right] \\
&= \sum_l \left[\left(\int \delta b(y)\, \overline{\eta_l(y)}\, \mathrm{d}y\right) \eta_l(y)\right] \\
&= \sum_l \left(\delta b_0\, \eta_l(y_0)\right) \\
&\approx \delta b_0 \eta_{l_0}(y_0),
\end{aligned} \tag{45}
$$

where $l_0$ is the index of the steering point closest to $y_0$. Thus, with this normalization an isotropic point scatterer will produce an image corresponding to the induced (and spatially localized) sensitivity function weighted by the strength of the scatterer (see, e.g., Figure 6), which lends itself to interpretation and analysis. Also note that other types of normalization (e.g., $||\cdot||_2$) are possible in a different context.

One important point to note is that the matrix $\Sigma_{\mathcal{B}}$, although observed to be generally invertible in our numerical experiments, can be ill-conditioned. For this reason, we generally resort to the use of the pseudoinverse $\Sigma_{\mathcal{B}}^{\dagger}$, where

$$
\left[\Sigma_{\mathcal{B}}^{\dagger}\right]_{ii} = \begin{cases} [\Sigma_{\mathcal{B}}]_{ii}^{-1} & \text{if } [\Sigma_{\mathcal{B}}]_{ii} \geq \sigma_\tau, \\ 0 & \text{otherwise.} \end{cases} \tag{46}
$$

The choice of the threshold $\sigma_\tau$ depends on two things: resolution and noise. As discussed in detail in section 4.1, there exists a trade-off between the two: the larger the threshold, the lesser the resolution but the greater the robustness to noise and vice versa.

**Algorithm 2** Filter computation.

Inputs: $G$ (a single steering (good) point), $B$ (a set nulling (bad) points), $\sigma_\tau$ (regularization parameters)
Compute: $\mathcal{A}$, $\mathcal{B}$ (40)-(41)
Compute: $U_{\mathcal{B}}$, $S_{\mathcal{B}}$, $V_{\mathcal{B}} \leftarrow \mathrm{SVD}(\mathcal{B})$
**for** $i \in \{1, 2, \ldots, 6JN\}$ **do**
  $[\Sigma_{\mathcal{B}}^{\dagger}]_{ii} \leftarrow [S_{\mathcal{B}}]_{ii}^{-1}$ if $[S_{\mathcal{B}}]_{ii} > \sigma_\tau$ and 0 otherwise
**end for**
$M \leftarrow \mathcal{A} V_{\mathcal{B}} \Sigma_{\mathcal{B}}^{\dagger}$
$f \leftarrow$ principal eigenvector of $M^* M$
Normalize $f$ (44)
Output: $f$

### 4.1. Effects of noise.

In this section, we describe the effects of additive measurement noise on the quality of the images generated through our proposed scheme. For this purpose,

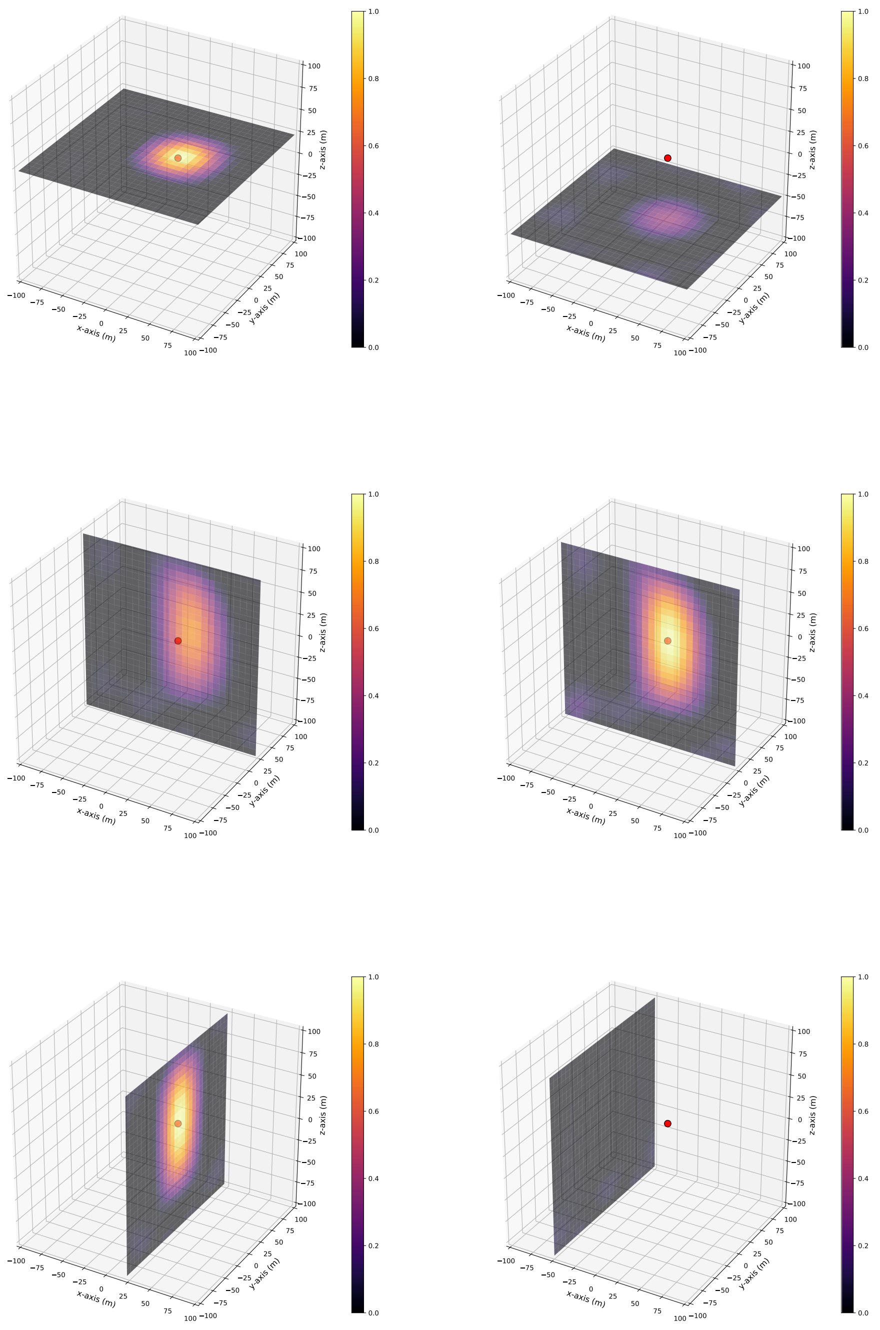


**Figure 6.** *Cross-sectional (2D) views of the (3D) image reconstructed using our proposed imaging scheme. Scatterer located at* $(22, 0, 22)$ *m between* $3 \times 3$ *source and receiver parallel arrays at* $z = \pm 150$ *m. From left to right, top to bottom: xy-plane,* $z = 22$ *m; xy-plane,* $z = -50$ *m; xz-plane,* $y = 22$ *m; xz-plane,* $y = 0$ *m; yz-plane,* $x = 22$ *m; yz-plane,* $x = -50$ *m. Both cross-range and range resolution are significantly superior to existing techniques.*

we define the SNR as

$$\text{SNR} = \frac{||d||^2}{\mathbb{E}\left[||\nu||^2\right]} = \frac{||d||^2}{N\sigma^2}, \tag{47}$$

where $\nu$ corresponds to a Gaussian noise vector with covariance $\sigma^2 I$, i.e., $\nu \sim \mathcal{N}(0, \sigma^2 I)$, and $N$ is the total number of measurements. Then, we have the following lemma (proved in Appendix A). In everything that follows, $||\cdot||_\infty$ refers to the maximum of the vector and $||\cdot||$ is the 2-norm of the vector.

Lemma 1 (quantification of noise effects). *Let $\nu$ be a zero-mean Gaussian random vector with covariance matrix $\sigma^2 I$, i.e., $\nu \sim \mathcal{N}(0, \sigma^2 I)$, and let*

$$R'[a,b]^* F(d+\nu) = \sum_{l=1}^{L} R'[a,b]^* \left(f_l f_l^*\right)(d+\nu) \tag{48}$$

*correspond to the image formation operator described in (36) applied to data (d) corrupted by noise ($\nu$). Assume further that the images of the filters $\{R'[a,b]^* f_l\}_{l=1}^{L}$ satisfy*

$$\left(R'[a,b]^* f_{l_1}\right)^* \left(R'[a,b]^* f_{l_2}\right) = 0 \tag{49}$$

*for $l_1 \neq l_2$. Then,*

$$\mathbb{P}\left(\left|\left|\sum_{l=1}^{L} R'[a,b]^* \left(f_l f_l^*\right) \nu\right|\right|^2 \geq \epsilon\, ||\mathcal{I}||_\infty^2\right) \leq \frac{\sigma^2}{\epsilon\, ||\mathcal{I}||_\infty^2} \sum_{l=1}^{L} ||f_l||^2, \tag{50}$$

*where $\mathcal{I} := \sum_{l=1}^{L} R'[a,b]^* \left(f_l f_l^*\right) d$ is the original noiseless image.*

Please refer to the appendix for a proof.

*Remark.* In practice, orthogonality in (49) does not always hold. However, when $l_1 \neq l_2$, the induced sensitivity functions are approximately supported on disjoint sets (localized around different steering points) in such a way that (49) holds approximately.

Now, we recall from (43) and (46) that

$$||f_l||_2^2 \sim \xi_l^* \left(\Sigma_{\mathcal{B}_l}^\dagger\right)^2 \xi_l \leq \sigma_\tau^{-2}, \tag{51}$$

where $\Sigma_{\mathcal{B}_l}^\dagger$ is the pseudoinverse of the diagonal matrix of singular values of the sensitivity matrix $\mathcal{B}_l$ associated with the $l$th steering point $x_l$. Therefore, Lemma 1 and the definition of SNR imply that

$$\mathbb{P}\left(\left|\left|\sum_{l=1}^{L} R'[a,b]^* \left(f_l f_l^*\right) \nu\right|\right|^2 \geq \epsilon\, ||\mathcal{I}||_\infty^2\right) \leq \frac{1}{\epsilon\, \text{SNR}\, ||\mathcal{I}||_\infty^2} \frac{||d||^2}{N} \sum_{l=1}^{L} \xi_l^* \left(\Sigma_{\mathcal{B}_l}^\dagger\right)^2 \xi_l \tag{52}$$

$$\leq \frac{1}{\epsilon\, \text{SNR}\, ||\mathcal{I}||_\infty^2} \frac{||d||^2}{N} \frac{L}{\sigma_\tau^2} \tag{53}$$

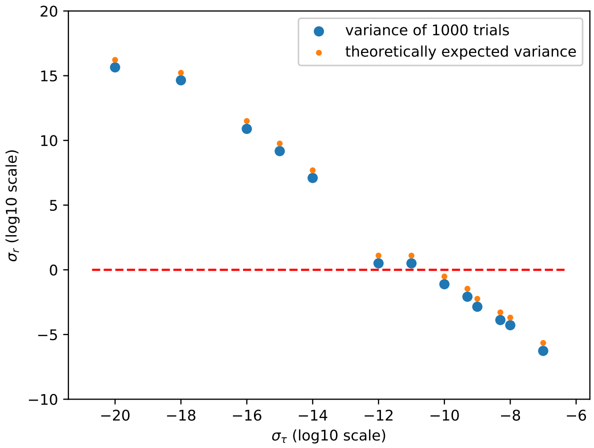


**Figure 7.** *Variance of the imaging scheme as a function of regularization paramter $\sigma_\tau$. The good point set $G$ corresponds to the origin, bad point set $B$ corresponding to a $19 \times 19 \times 19$ uniform grid (excluding the origin). This is with $z$-polarized dipole sources and $6$-axis receivers in the parallel array setup, and the frequency is $1000$ Hz. The "variance" plotted, $\sigma_r$, corresponds to the right-hand side of (52). The variance of $1000$ trials is the variance computed from $1000$ random vectors $\nu$, and the theoretical value is the value of the expression in this instance of $60$ dB of SNR. The geometry has a $4 \times 4$ xy-plane source and receiver arrays located at $z = \pm 150m$. To get the variance on the image to be less than the order of magnitude of the data, the smallest $\sigma_\tau$ that has $\sigma_r \ll 1$ should be chosen.*

from which we conclude that the probability that the relative energy of the noise induced in the image dominates that of the original image is bounded by a quantity proportional to the amount of regularization applied (higher regularization implies lower probability) and inversely proportional to the SNR. This behavior is commonly encountered in the field of imaging. Our derivation, however, provides explicit estimates in this particular context.

There is currently no known closed-form expression to describe the behavior of the singular values of the sensitivity matrices $\{\mathcal{B}_l\}$ as a function of the imaging parameters such as the location and number of sources and receivers, the orientation of the dipole sources, the background medium, etc. Further, a highly nontrivial relationship was observed through numerical experiments (section 5.2), an example of which is shown in Figure 7. We thus restrict ourselves to a computational approach in which we fix the imaging setup, compute the SVDs of $\{\mathcal{B}_l\}$, and pick $\sigma_\tau$ so that the left-hand side of (52) lies below some user-provided threshold $p$.

## 5. Numerical results.

In this section, we present extensive numerical results for the performance and capabilities of our imaging scheme. The section contains four subsections:

- Section 5.1 provides comparison with common techniques (section 1.1) and shows that the proposed imaging scheme offers significant resolution improvements over those competitors.
- Section 5.2 addresses the effects of noise described in section 4.1 from a numerical standpoint.
- Section 5.3 discusses a case of low-frequency imaging in a highly inhomogeneous medium, namely, a finite conductor located within a conducting box.

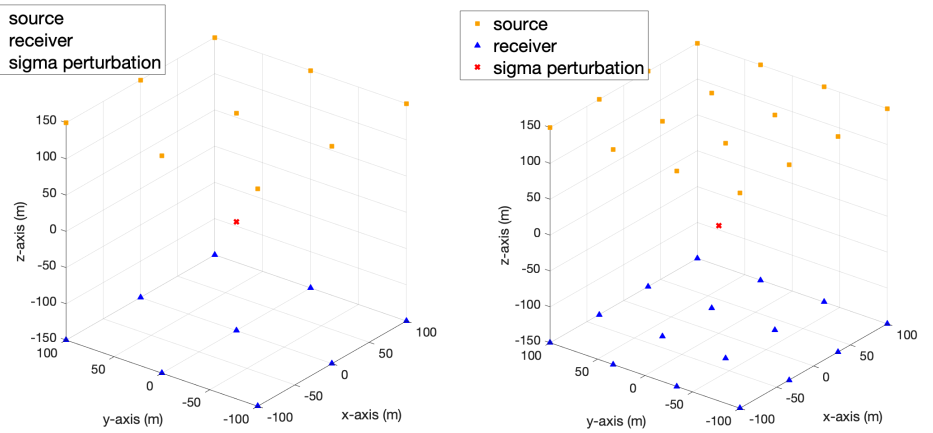


**Figure 8.** *Backlit, parallel linear arrays imaging setup with* $3 \times 3$ *or* $4 \times 4$ *sources and receiver arrays.*

- Section 5.4 presents "resolution maps," which provide a methodology for quantifying the spatially dependent resolution achievable with the proposed scheme under specific imaging configurations.

Unless otherwise stated, all examples use a frequency of $f = 1$ kHz ($\lambda \approx 300$ km), and all necessary wave propagation simulations are computed using the algorithm introduced in section 3 with a stopping criterion of $\delta = 10^{-8}$. Scatterers are assumed to be isotropic point perturbations (Dirac delta) in conductivity only; i.e., $\sigma(x) = \sum_{n=1}^{N} \sigma_n I_{3\times3}\, \delta(x - x_n)$. The imaging configuration consists of a backlit, parallel linear arrays imaging setup (Figure 8) made up of square arrays of sources (orange cubes) and receivers (blue triangles) perpendicular to the $z$-axis, and located at $z = \pm 150$ m, respectively. Sources are ideal dipoles, and receivers are assumed to be noise-free (SNR $= \infty$) and capable of measuring all six components of the electromagnetic field. Finally, a homogeneous background corresponds to a medium with the properties of free space: $\epsilon(x) = \epsilon_0 = 8.854187 \cdot 10^{-12}$ F/m , $\mu(x) = \mu_0 = 1.256637 \cdot 10^{-6}$ H/m, $\sigma(x) = 0$ S/m.

**5.1. Comparison with existing techniques.** In this section, we compare our proposed scheme with two commonly encountered low-frequency imaging schemes: output least squares with Tikhonov regularization [6] and nonlinear block-Kaczmarz output least squares (section 1.1). In these examples, a single conductive scatterer with strength $\sigma_0 = 1\,$S/m is located at $(22, 0, 22)$ in a homogeneous background.

The results are displayed in Figures 5–6 which shows six cross-sectional (2D) views of the reconstructed (3D) image for each case under considerations. As can be seen, both the output least squares and the Kaczmarz method (Figures 5–9) produce very similar outputs that provide relatively low cross-range resolution and no range resolution (in fact, the location of highest intensity in the range direction is closest to the receiver array, which is completely erroneous). On the contrary, our proposed method generates images with significantly better cross-range resolution and range resolution (Figure 6).

It is important to note that these comparisons are done on the basis of a single (outer) iteration, whereas it has been shown in [15] that multiple outer iterations (sweeps) can improve

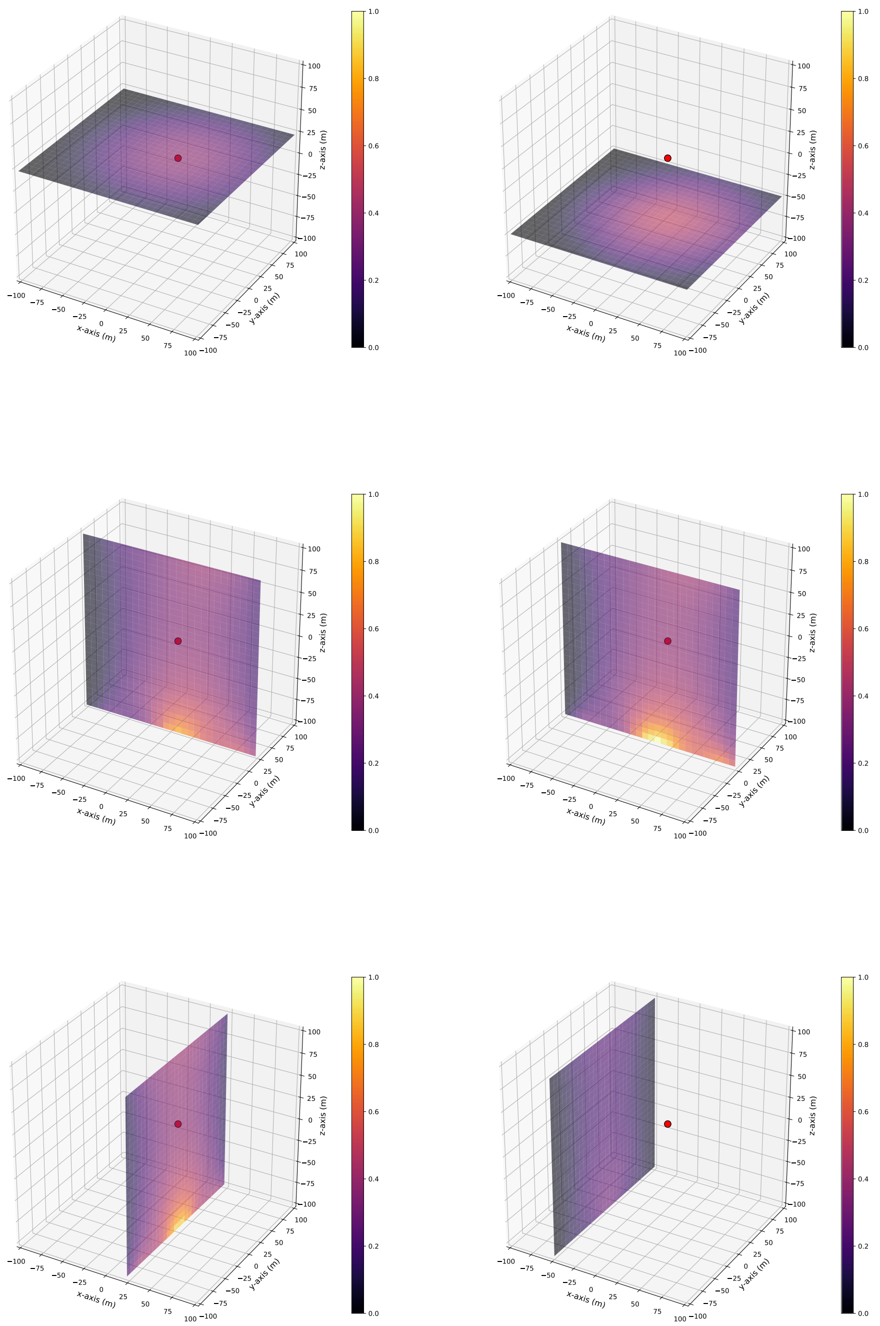


**Figure 9.** *Cross-sectional (2D) views of the (3D) image reconstructed using the block-Kaczmarz (single-sweep) nonlinear output least squares* [15, 16]*. Scatterer located at* $(22, 0, 22)\,m$ *between* $3\times3$ *source and receiver parallel arrays at* $z = \pm150$ *m. From left to right, top to bottom: xy-plane,* $z = 22$ *m; xy-plane,* $z = -50$ *m; xz-plane,* $y = 22$ *m; xz-plane,* $y = 0$ *m; yz-plane,* $x = 22$ *m; yz-plane,* $x = -50$ *m. Cross-range resolution is poor. There is no range resolution. This is qualitatively similar to the results displayed in Figure* 5.

the results. In this sense, we wish to underline two points: first, the results found in [15] pertain to cross-range resolution; no numerical results have demonstrated range resolution. Second, although the paper focuses on a single-step imaging, our method also lends itself to an iterative descent framework for nonlinear inversion as described in section 2.1.

Finally, it should also be noted that our technique provides better cross-range resolution than range resolution in this parallel array setup. This is expected, at least qualitatively, given the discussion of section 4 and the nature of the sensitivity functions (Figure 4(b), right). Section 4 also elucidates the nature of the image obtained through the least-squares and Kaczmarz methods (Figure 4(b), left). Finally, the fact that the output least-squares and the Kaczmarz methods generate similar images can be explained by the fact that, in this particular setup, the approximation in (20) is an appropriate one.

**5.2. Effects of noise.** Here, we provide numerical examples and describe the effects of additive noise on image quality and resolution. To do so, we consider the $4 \times 4$ planar array setup as shown in Figure 8.

Our simulations are based on (52); first, we fix the imaging setup (Figure 8). We numerically generate data for a single scatterer at the origin, and add Gaussian noise to reach an SNR level of 60 dB. Then, we construct filters based on Algorithm 2 for various threshold values, i.e., $\sigma_\tau \in \{10^{-9}, 10^{-10}, 10^{-20}\}$. Finally, we proceed to the imaging following Algorithm 1. The results of the numerical simulations are shown in Figures 10–11.

The regularizing threshold values $(\sigma_\tau)$ were chosen according to the methodology described in section 4.1 and the behavior of the singular values of the sensitivity matrices shown in Figure 7. The value $\sigma_\tau = 10^{-10}$ (Figure 11) corresponds to an "underregularized" case, whereas the value $\sigma_\tau = 10^{-9}$ (Figure 12) is appropriately regularized. Correspondingly, it is seen that the underregularized case produces a highly noisy image with very poor localization compared to the other two cases. Further, it becomes apparent from looking at Figures 10–12 that the amount of regularization has a significant impact on the achievable resolution. Better resolution is obtained in the infinite SNR case in which lower regularization was possible as discussed in section 4.1.

**5.3. Inhomogeneous background.** We now discuss low-frequency imaging in an inhomogeneous medium. For this purpose, we consider a background consisting of a thick conductive box with one open side (Figure 13). The box is square and of dimensions $176 \times 176 \times 176$ m with walls approximately 16 m thick. The conductivity of the box material is 1 S/m. It is assumed that all corners and sides are sealed and smooth, with the exception of the open face.[10] The scatterer to be imaged corresponds to a Gaussian with a standard deviation of 8 m centered at $(0, 20, 20)$ m and having maximum conductivity of $10^3$ S/m. The imaging setup consists of 25 sources and 25 receivers distributed uniformly at random on a sphere of radius 180 m (full aperture). The sources have coordinates $x < 0$ and the receivers have coordinates $x > 0$. Sources are randomly oriented magnetic dipoles, and receivers can measure all 6 components of the electromagnetic field.

We note that the properties of the box walls imply a skin depth of approximately 16 m at $10^3$ Hz, and 2 m at $10^9$ Hz. This means that the low-frequency waves employed here can

[10] This is an idealization since realistic structures are generally corrugated and have various types of gaps.

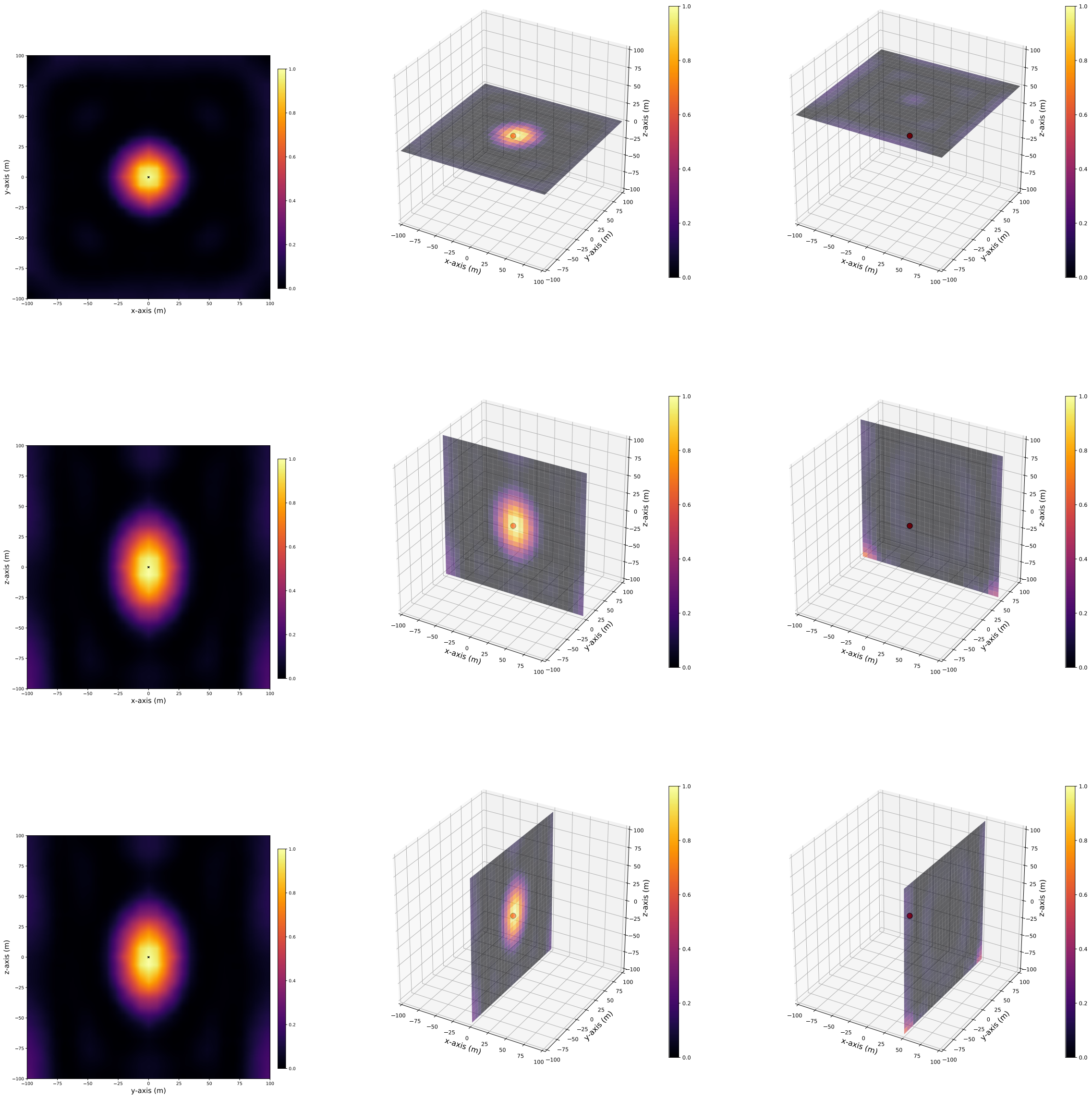


**Figure 10.** *Imaging process applied to uncorrupted data. Single conductivity scatterer at the origin.* SNR $=\infty$, $4\times 4$ *sources/receivers arrays (Figure 8). The scatterer can be appropriately localized.*

penetrate through the wall and provide a full-aperture view of the scatterer. Typical high-frequency imaging using millimeter waves (radar) would see emitted pulses either bounce off the wall or enter the box through the opening only to undergo multiple scattering once inside, thus making existing (linear) high-frequency imaging techniques inadequate.

For these imaging examples, efficient algorithms for solving Maxwell's equations were vital. Computing the residual vector requires solutions of as many problems as there are sources. In

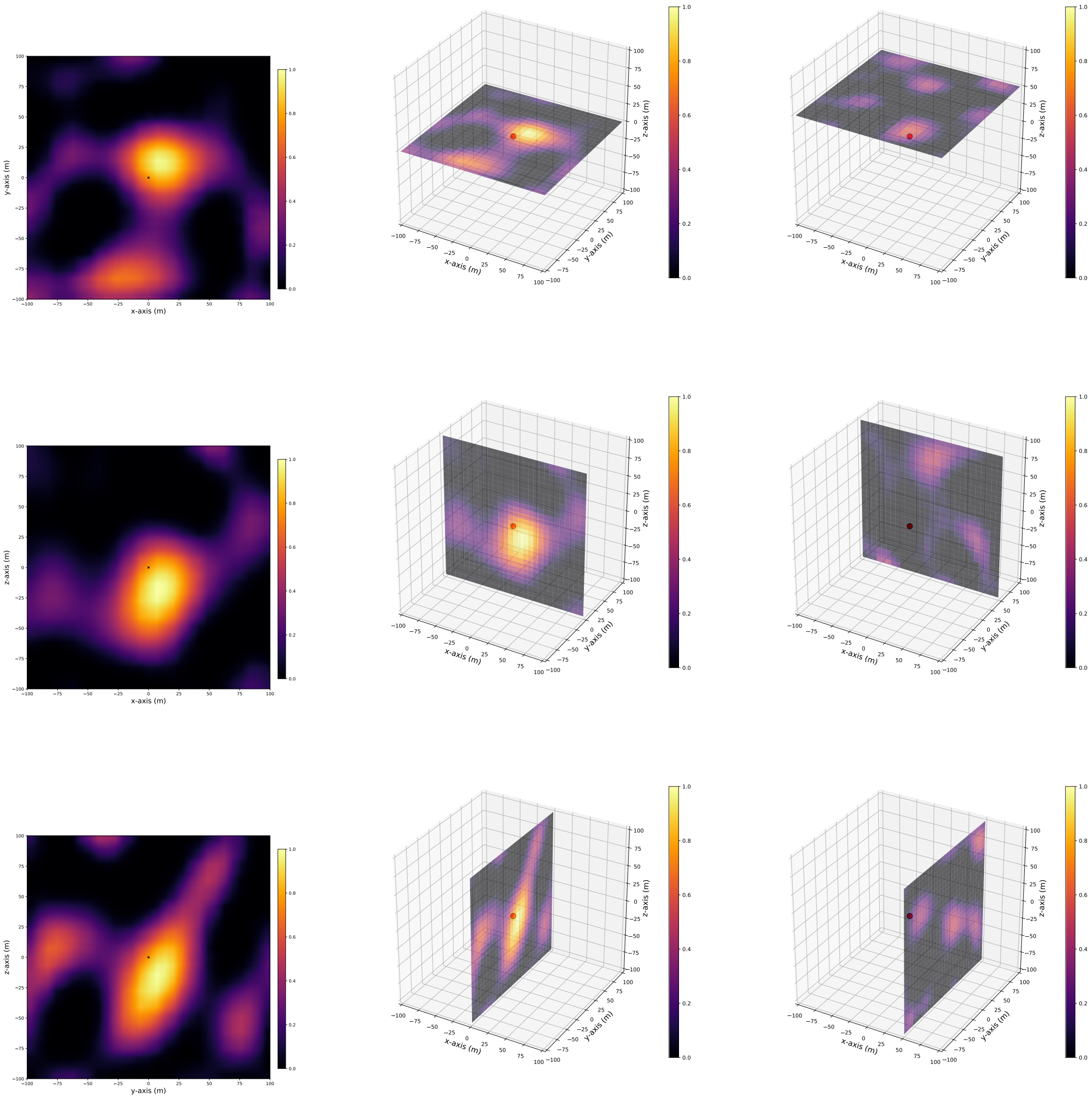


**Figure 11.** *Imaging process applied to Gaussian noise-corrupted data. Single conductivity scatterer at the origin.* SNR $= 60$ *dB, regularization parameter* $\sigma_\tau = 10^{-10}$*,* $4 \times 4$ *sources/receivers arrays (Figure 8). The image is noisy and the scatterer can no longer be localized due to an inappropriate amount of regularization.*

this case, there were 25. Further, the sensitivity functions for each source and each receiver component of every receiver needed calculation. For this problem that is $25 + 6 \cdot 25 = 175$ problems. Every one of these problems was solved on a grid of $50 \times 50 \times 50$ voxels, each possessing $6 \cdot 25^3 \approx 10^5$ unknowns.

Results are shown in Figure 14 which compares the image obtained in the absence (left) and presence (right) of the box, respectively. In these simulations, LGMRES was used with a

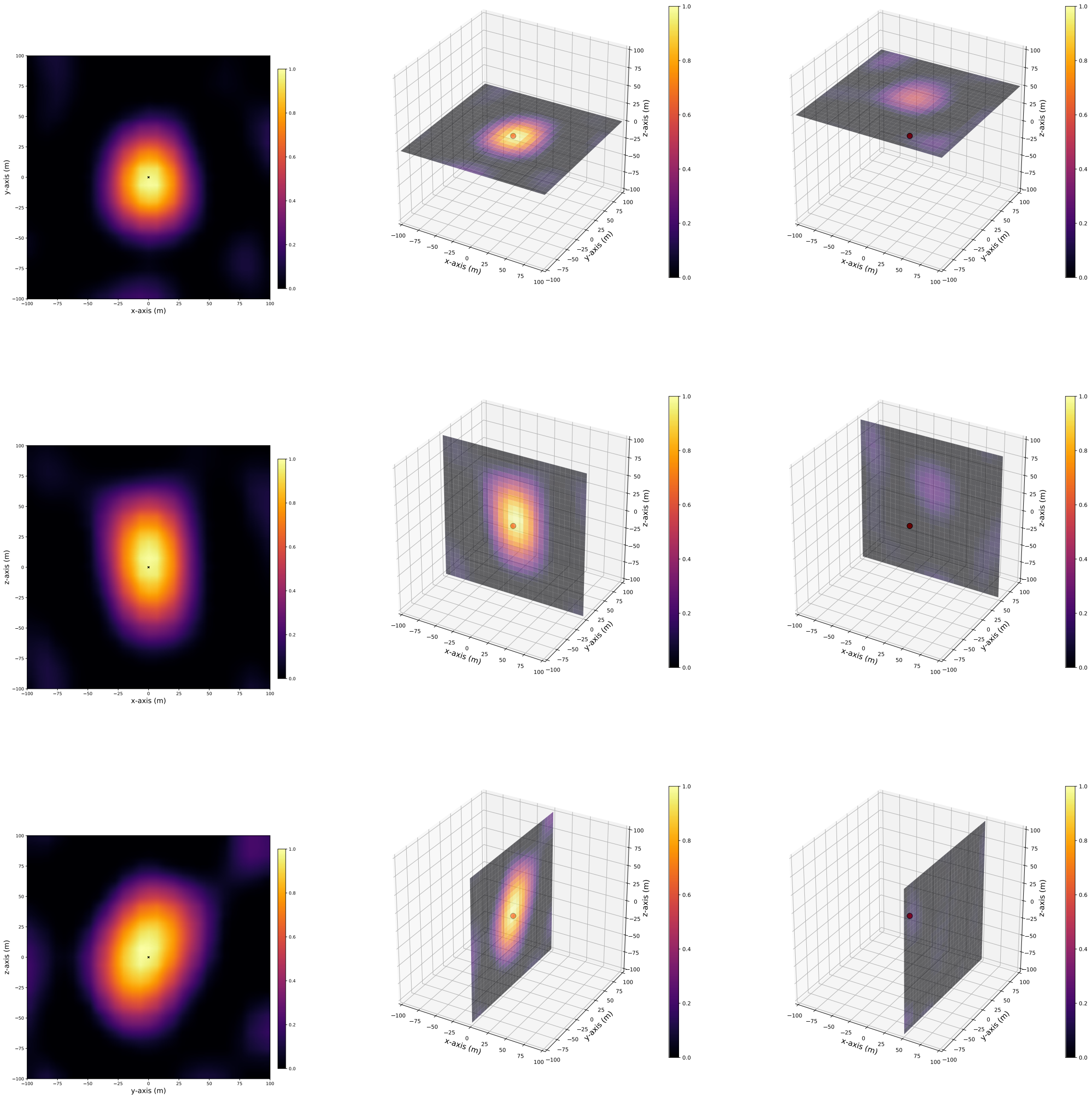


**Figure 12.** *Imaging process applied to Gaussian noise-corrupted data. Single conductivity scatterer at origin.* SNR $= 60$ *dB, regularization parameter* $\sigma_\mathcal{T} = 10^{-9}$*,* $4 \times 4$ *sources/receivers arrays (Figure 8). The scatterer can be appropriately localized, but the resolution is poorer due to the regularization.*

tolerance of $10^{-14}$ and the regularization parameter $\sigma_\mathcal{T}$ was set to $10^{-8}$. Our first conclusion is that it is indeed possible to localize a scatterer within a conductive structure using low-frequency waves. We also notice that the resolution of the image in the presence of the box is only slightly poorer than that obtained in a homogeneous medium, leading us to conclude that resolution is more likely to be affected by noise, as previously observed, than by known penetrable structures.

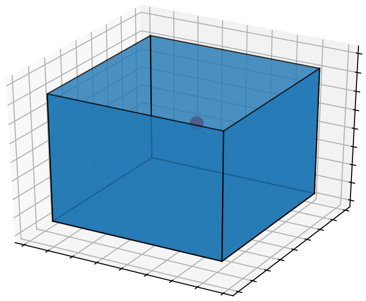

**Figure 13.** *A conductive 3D square enclosure with the top wall removed, corresponding to the structure used in section 5.3; $176 \times 176 \times 176$ $m^3$, 16 m-thick walls of conductivity 1 S/m.*

Finally, it is worth mentioning that although the structure was assumed to be known in this example, this is not necessary for the scheme to succeed; unknown elements in a structure will appear as perturbations/scatterers in our image.

**5.4. Resolution Maps.** In this final section, we introduce the notion of a *resolution map*. In short, a resolution map provides a pointwise estimate of the best resolution achievable through our proposed technique. Here, by resolution at a point we mean the minimum distance between a scatterer at this particular point and any other scatterer such that they can be distinguished.[11] In particular, we note that this concept becomes equivalent to the traditional concept of resolution, or Rayleigh criterion, as the wavelength goes to zero (high-frequency asymptotics). At low frequency, however, we find that resolution exhibits interesting properties such as spatial and directional dependence.

The methodology for creating a resolution map is relatively simple and can be described as follows: given some background medium properties $\epsilon(x)$, $\mu(x)$, and $\sigma(x)$ and a set of points where one would like to know the resolution (e.g., a fine regular grid), compute a filter as described in section 4 (Algorithm 2) for each such point and plot the induced sensitivity function $\eta(x)$ (34). Then, given a resolution level $0 < \gamma < 1$ corresponding to the percentage of the maximum of the filter centered $x_0$ below which its value is considered negligible (we pick $\gamma = 0.5$ in our examples) and a unit direction vector $\vec{d}$, the resolution at $x_0$ is defined as,

$$\lambda_{\gamma,\vec{d}}(x_0) = \sup_x \left\{ \vec{d} \cdot (x - x_0) \, : \, \left| \phi \left( x_0 + (\vec{d} \cdot (x - x_0)) \, \vec{d} \right) \right| \geq \gamma \, |\phi(x_0)| \right\}. \tag{54}$$

Resolution maps for a homogeneous background with $3 \times 3$ parallel arrays are shown in Figure 15, demonstrating, among other things, that better resolution is achieved for steering points closer to the source and/or receiver arrays, and that the resolution exhibits a complex spatially dependent behavior.

[11] This concept of resolution requires that the single-scattering, or Born, approximation holds among scatterers, but not between the scatterers and the background.

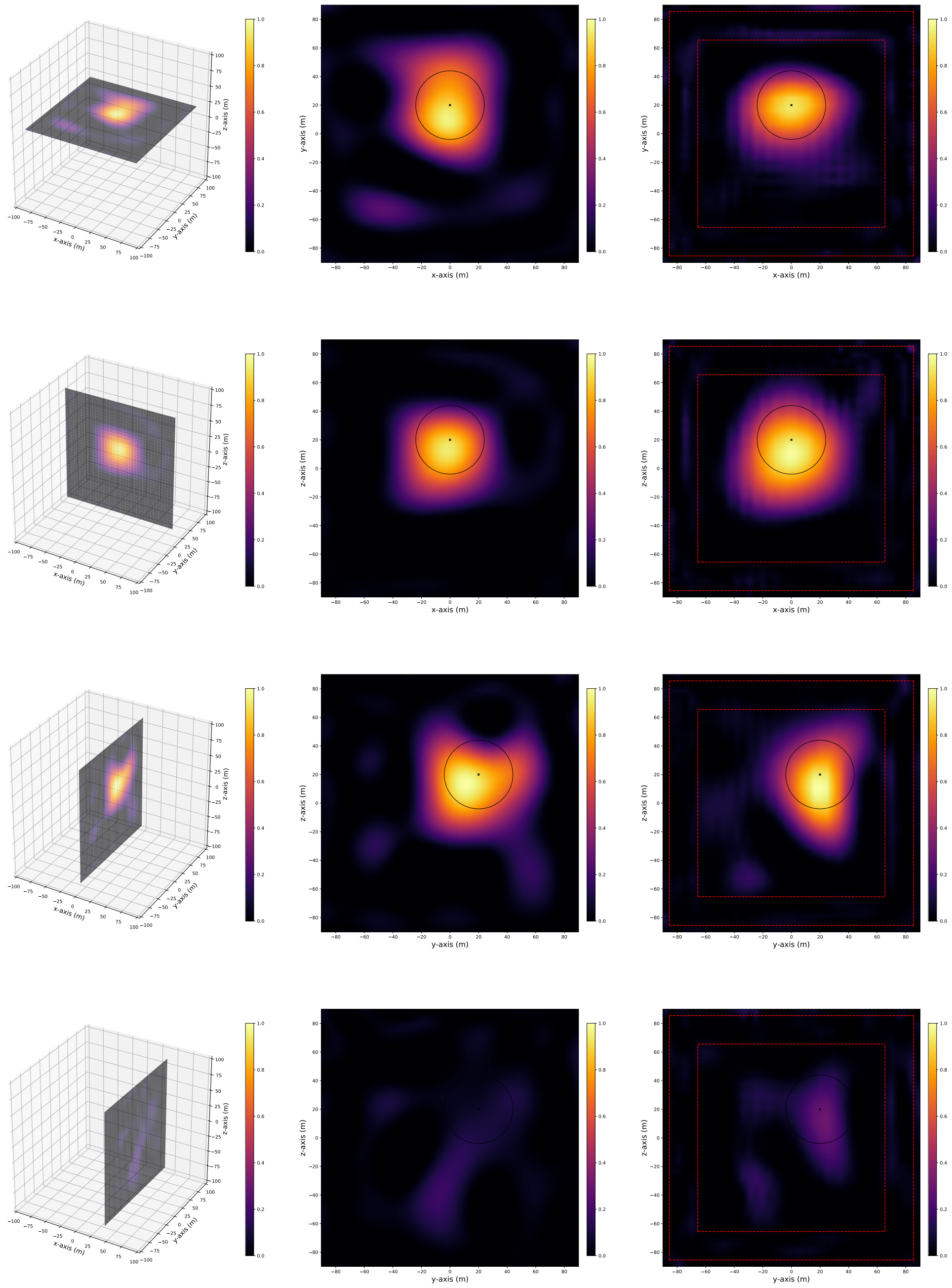

**Figure 14.** *Imaging process applied to a conductive spherical scatterer located at* $(0, 20, 20)$ *m inside a conductive square box of dimension* $176 \times 176 \times 176$ *m-centered at the origin and possessing* $20$ *m-thick walls (red dashed line). Left:* $3D$ *cross sections, no conductive box. Middle:* $2D$ *cross sections, no conductive box. Right:* $2D$ *cross sections, conductive box. The red dashed line delineates the boundary of the box. The resolution achieved in the presence of the box is similar to the resolution achieved in its absence.*

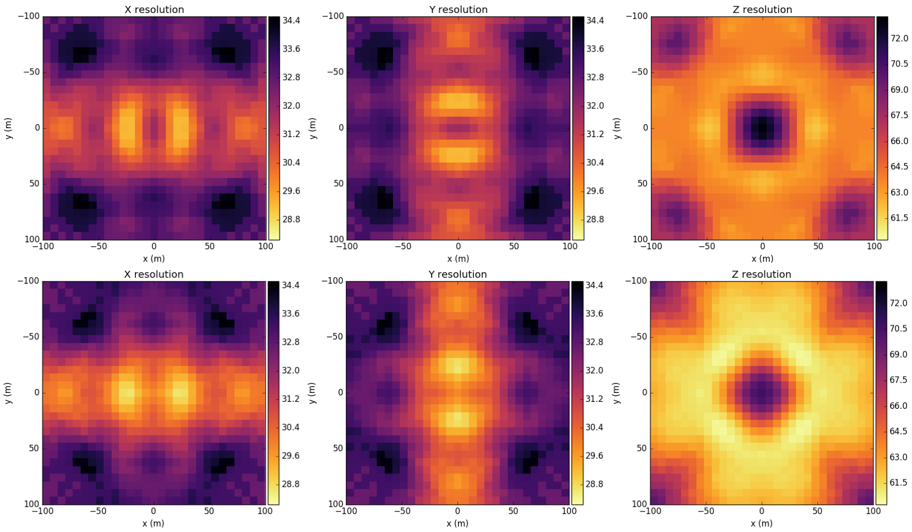


**Figure 15.** *Resolution map with homogeneous background medium. Parallel arrays $3 \times 3$ source/receiver arrays imaging configuration located in the xy-plane at $z = \pm 150$ m. Left to right: resolution along the x-, y-, and z-direction. Top: xy-plane, $z = 0$ m. Bottom: xy-plane, $z = 40$ m.*

## 6. Conclusion.

In conclusion, we have introduced a novel scheme based on a recently developed fast algorithm for the simulation of electromagnetic waves traveling through complex 3D media for the purpose of 3D imaging using low-frequency electromagnetic waves that shows superior computational performance and improved resolution over existing techniques. Finally, we numerically demonstrated the improved resolution of the proposed technique over existing techniques, studied the effects of noise, introduced a resolution map methodology, and provided imaging results in complex media for which existing high-frequency techniques are deemed inadequate.

Future directions include applications to a wider array of problems, simultaneous treatment of multimedia imaging (conductivity, permittivity, and permeability), refinement of the steering points localization through the use of resolution maps, as well as improvement to the fast algorithms for 3D electromagnetic wave simulations both from a theoretical and software implementation perspective, especially on distributed platforms.

## Appendix A. Lippmann–Schwinger framework.

Theorem 3 **(Lippmann–Schwinger framework).** *Consider*

(55)
$$A_{11}(Q(x)) = -i\omega\mu_0 \int \overleftrightarrow{G}(x,y)\, \tilde{b}(y)\, Q(y)\mathrm{d}y, \quad A_{12}(Q(x)) = \int \nabla \times \overleftrightarrow{G}(x,y)\, (-\tilde{a}(y))\, Q(y)\mathrm{d}y,$$

(56)
$$A_{21}(Q(x)) = \int \nabla \times \overleftrightarrow{G}(x,y)\, \tilde{b}(y)\, Q(y)\mathrm{d}y, \qquad A_{22}(Q(x)) = i\omega\epsilon_0 \int \overleftrightarrow{G}(x,y)\, (-\tilde{a}(y))\, Q(y)\mathrm{d}y,$$

*where $\tilde{a}(x) = i\omega\,(\mu(x) - \mu_0)$ and $\tilde{b}(x) = i\omega\,(\epsilon(x) - \epsilon_0) + \sigma(x)$. Then, the solution to (7) is* *characterized by the linear system*

$$\begin{bmatrix} E(x) \\ H(x) \end{bmatrix} = \begin{bmatrix} E_0(x) \\ H_0(x) \end{bmatrix} + \begin{bmatrix} A_{11} & A_{12} \\ A_{21} & A_{22} \end{bmatrix} \begin{bmatrix} E(x) \\ H(x) \end{bmatrix} = \begin{bmatrix} E_0(x) \\ H_0(x) \end{bmatrix} + A \begin{bmatrix} E(x) \\ H(x) \end{bmatrix}, \tag{57}$$

*where* $\overleftrightarrow{G}(x,y)$ *is the dyadic Green's function of* (27)*, and*

$$\begin{aligned} E_0 &= -i\omega\mu_0 \int \overleftrightarrow{G}(x,y)\, J(y)\, \mathrm{d}y + \int \nabla \times \overleftrightarrow{G}(x,y)\, M(y)\, \mathrm{d}y, \\ H_0 &= \int \nabla \times \overleftrightarrow{G}(x,y)\, J(y)\, \mathrm{d}y + i\omega\epsilon_0 \int \overleftrightarrow{G}(x,y)\, M(y)\, \mathrm{d}y, \end{aligned} \tag{58}$$

*corresponds to the incoming field in a homogeneous background medium.*

*Proof.* First, introduce,

$$\tilde{a}(x) = i\omega\mu(x) - i\omega\mu_0, \tag{59}$$

$$\tilde{b}(x) = i\omega\epsilon(x) + \sigma(x) - i\omega\epsilon_0, \tag{60}$$

and rewrite Maxwell's equations (7) as

$$\begin{cases} \nabla \times H(x) - i\omega\epsilon_0 E(x) = J(x) + \tilde{b}(x)\, E(x), \\ \nabla \times E(x) + i\omega\mu_0 H(x) = M(x) - \tilde{a}(x)\, H(x). \end{cases} \tag{61}$$

Split the resulting system of equations into two linear systems with different right-hand sides to get

$$\begin{cases} \nabla \times H^{(1)}(x) - i\omega\epsilon_0 E^{(1)}(x) = J(x) + \tilde{b}(x)\, E^{(1)}(x), \\ \nabla \times E^{(1)}(x) + i\omega\mu_0 H^{(1)}(x) = 0, \end{cases} \tag{62}$$

$$\begin{cases} \nabla \times H^{(2)}(x) - i\omega\epsilon_0 E^{(2)}(x) = 0, \\ \nabla \times E^{(2)}(x) + i\omega\mu_0 H^{(2)}(x) = M(x) - \tilde{a}(x)\, H^{(2)}(x). \end{cases} \tag{63}$$

From linearity we have that

$$\begin{aligned} E(x) &= E^{(1)}(x) + E^{(2)}(x), \\ H(x) &= H^{(1)}(x) + H^{(2)}(x). \end{aligned}$$

Below, we derive the explicit form of $E^{(1)}(x)$ and $H^{(1)}(x)$. The expressions for $E^{(2)}(x)$ and $H^{(2)}(x)$ can be obtained analogously. Our starting point for the latter purpose is an ansatz of the form,[12]

$$E(x) = i\omega A(x) - \nabla\phi(x), \tag{64}$$

$$H(x) = -\frac{1}{i\omega\mu_0}\nabla \times E(x) = -\frac{1}{\mu_0}\nabla \times A(x), \tag{65}$$

[12] This is known as the Helmholtz decomposition for vector fields. Every sufficiently regular vector field in $\mathbb{R}^3$ can be written as such [42].

where the expression for $H(x)$ is obtained using the second equation in system (62). Substituting (65) into the first equation of system (62) leads to,

$$\nabla \times \nabla \times A(x) - \omega^2 \epsilon_0 \mu_0 A(x) - i\omega\epsilon_0\mu_0 \nabla\phi(x) = -\mu_0 \left(J(x) + \tilde{b}(x)E(x)\right).$$

Introduce the Lorentz gauge,

$$\nabla \cdot A(x) = i\omega\epsilon_0\mu_0\, \phi(x), \tag{66}$$

and substitute to get,

$$\nabla \times \nabla \times A(x) - \nabla\nabla \cdot A(x) - \omega^2\epsilon_0\mu_0 A(x) = -\left(\nabla^2 A(x) + k^2 A(x)\right) = -\mu_0 \left(J(x) + \tilde{b}(x)E(x)\right)$$

after using the identity $\nabla\times\nabla\times A(x) - \nabla\nabla\cdot A(x) = -\nabla^2 A(x)$, and recalling that: $k^2 = \omega^2\epsilon_0\mu_0$. This expression holds componentwise which implies that each component satisfies the scalar Helmholtz equation,

$$\left(\nabla^2 + k^2\right) G(x) = -\delta(x), \tag{67}$$

whose fundamental solution is given by: $G(x) = \frac{e^{ik|x|}}{4\pi|x|}$. Therefore,

$$A(x) = -\int \overleftrightarrow{I}\, G(x-y)\, \mu_0 \left(J(x) + \tilde{b}(x)E(x)\right) \mathrm{d}y, \tag{68}$$

$$\begin{aligned} \phi(x) &= -\frac{1}{\mu_0\,(i\omega\epsilon_0)} \int \nabla \cdot \left(\overleftrightarrow{I} G(x-y)\, \mu_0 \left(J(x) + \tilde{b}(x)E(x)\right)\right) \mathrm{d}y \\ &= -\frac{1}{i\omega\epsilon_0} \int \nabla G(x-y) \left(J(x) + \tilde{b}(x)E(x)\right) \mathrm{d}y, \end{aligned} \tag{69}$$

following (66), and since $\nabla \cdot (\overleftrightarrow{I}\, G(x)) = \nabla G(x)$. Substitution into (64)–(65) leads to

$$\begin{aligned} E^{(1)}(x) &= i\omega \left(-\int \overleftrightarrow{I}\, G(x-y)\, \mu_0 \left(J(x) + \tilde{b}(x)E(x)\right) \mathrm{d}y\right) \\ &\quad - \nabla\left(-\frac{1}{i\omega\epsilon_0} \int \nabla G(x-y) \left(J(x) + \tilde{b}(x)E(x)\right) \mathrm{d}y\right) \\ &= -i\omega\mu_0 \left(\int \overleftrightarrow{I}\, G(x-y) \left(J(x) + \tilde{b}(x)E(x)\right) \mathrm{d}y \right. \\ &\quad \left. + \frac{1}{k^2} \int \nabla\nabla G(x-y) \left(J(x) + \tilde{b}(x)E(x)\right) \mathrm{d}y\right) \\ &= -i\omega\mu_0 \int \overleftrightarrow{G}(x,y) \left(J(x) + \tilde{b}(x)E(x)\right) \mathrm{d}y, \\ H^{(1)}(x) &= -\frac{1}{\mu_0}\nabla \times \left(-\int G(x-y)\, \mu_0 \left(J(x) + \tilde{b}(x)E(x)\right) \mathrm{d}y\right) \\ &= \int \nabla \times \overleftrightarrow{G}(x,y) \left(J(x) + \tilde{b}(x)E(x)\right) \mathrm{d}y, \end{aligned} \tag{70}$$

and the result follows. ∎

**Appendix B. Proof of Lemma 1.** First note that

$$\left(\sum_{l=1}^{L} R'[a,b]^* f_l f_l^*\right)\nu \sim \mathcal{N}\left(0, \sigma^2 \left(\sum_{l=1}^{L}(R'[a,b]^* f_l f_l^*\right)\left(\sum_{l=1}^{L} R'[a,b]^* f_l f_l^*\right)^*\right). \tag{71}$$

However,

$$\left(\sum_{l=1}^{L} R'[a,b]^* f_l f_l^*\right)\left(\sum_{m=1}^{L} R'[a,b]^* f_m f_m^*\right)^* = \sum_{l,m=1}^{L}(f_l^* f_m)\left(\sum_{l=1}^{L} R'[a,b]^* f_l\right)\left(\sum_{l=1}^{L} R'[a,b]^* f_m\right)^*. \tag{72}$$

In particular, this implies

$$\mathbb{E}\left[\left|\left|\left(\sum_{l=1}^{L} R'[a,b]^* f_l f_l^*\right)\nu\right|\right|^2\right] = \mathrm{Tr}\left(\sigma^2 \sum_{l,m=1}^{L}(f_l^* f_m)\left(\sum_{l=1}^{L} R'[a,b]^* f_l\right)\left(\sum_{l=1}^{L} R'[a,b]^* f_m\right)^*\right) \tag{73}$$

$$= \sigma^2 \sum_{l,m=1}^{L}(f_l^* f_m)\,\mathrm{Tr}\left(\left(\sum_{l=1}^{L} R'[a,b]^* f_l\right)^*\left(\sum_{l=1}^{L} R'[a,b]^* f_m\right)\right) \tag{74}$$

$$= \sigma^2 \sum_{l=1}^{L} ||f_l||^2 \tag{75}$$

following the orthogonality assumption and thanks to the linearity and cyclic properties of the trace. Therefore,

$$\mathbb{P}\left(\left|\left|\sum_{l=1}^{L} R'[a,b]^*\ (f_l f_l^*)\ \nu\right|\right|^2 \geq \epsilon\, ||\mathcal{I}||_\infty^2\right) \leq \frac{\sigma^2}{\epsilon\, ||\mathcal{I}||_\infty^2}\sum_{l=1}^{L} ||f_l||^2 \tag{76}$$

by the Chebyshev inequality. This is the desired result.

## REFERENCES


[1] H. Ammari, J. Chen, Z. Chen, J. Garnier, and D. Volkov, *Target detection and characterization from electromagnetic induction data*, J. Math. Pures Appl. (9), 101 (2014), pp. 54–75.

[2] S. Andrieux, T. Baranger, and A. B. Abda, *Solving Cauchy problems by minimizing an energy-like functional*, Inverse Problems, 22 (2006), 115.

[3] J.-F. Aubry, M. Tanter, J. Gerber, J.-L. Thomas, and M. Fink, *Optimal focusing by spatio-temporal inverse filter.* II. *Experiments. Application to focusing through absorbing and reverberating media*, J. Acoust. Soc. Am., 110 (2001), pp. 48–58.

[4] A. H. Baker, E. R. Jessup, and T. Manteuffel, *A technique for accelerating the convergence of restarted GMRES*, SIAM J. Matrix Anal. Appl., 26 (2005), pp. 962–984.

[5] J. G. Berryman and R. V. Kohn, *Variational constraints for electrical-impedance tomography*, Phys. Rev. Lett., 65 (1990), pp. 325–328.

[6] L. Borcea, *Electrical impedance tomography*, Inverse problems, 18 (2002), R99.

[7] L. Borcea, T. Callaghan, J. Garnier, and G. Papanicolaou, *A universal filter for enhanced imaging with small arrays*, Inverse Problems, 26 (2009), 015006.

[8] L. Borcea, G. A. Gray, and Y. Zhang, *Variationally constrained numerical solution of electrical impedance tomography*, Inverse Problems, 19 (2003), pp. 1159–1184.
[9] A. Borges, J. De Oliveira, J. Velez, C. Tavares, F. Linhares, and A. Peyton, *Development of electromagnetic tomography (EMT) for industrial applications. Part 2: Image reconstruction and software framework*, in Proceedings of the 1st World Congress on Industrial Process Tomography, Buxton Press, Buxton, England, 1999, pp. 219–225.
[10] A. Borsic, B. M. Graham, A. Adler, and W. R. Lionheart, *In vivo impedance imaging with total variation regularization*, IEEE Trans. Med. Imaging, 29 (2010), pp. 44–54.
[11] S. Brooks, A. Gelman, G. Jones, and X.-L. Meng, *Handbook of Markov Chain Monte Carlo*, CRC, Boca Raton, FL, 2011.
[12] V. Chitturi and F. Nagi, *Spatial resolution in electrical impedance tomography: A topical review*, J. Electr. Bioimped., 8 (2017), pp. 66–78.
[13] D. Colton and R. Kress, *Inverse Acoustic and Electromagnetic Scattering Theory*, Appl. Math. Sci. 93, Springer, New York, 2012.
[14] Z. Cui, Q. Wang, Q. Xue, W. Fan, L. Zhang, Z. Cao, B. Sun, H. Wang, and W. Yang, *A review on image reconstruction algorithms for electrical capacitance/resistance tomography*, Sensor Rev., 36 (2016), pp. 429–445.
[15] O. Dorn, H. Bertete-Aguirre, J. Berryman, and G. Papanicolaou, *A nonlinear inversion method for 3D electromagnetic imaging using adjoint fields*, Inverse Problems, 15 (1999), pp. 1523–1558.
[16] O. Dorn, H. Bertete-Aguirre, J. Berryman, and G. Papanicolaou, *Sensitivity analysis of a nonlinear inversion method for 3D electromagnetic imaging in anisotropic media*, Inverse Problems, 18 (2002), pp. 285–318.
[17] M. M. Dunlop, M. A. Iglesias, and A. M. Stuart, *Hierarchical Bayesian level set inversion*, Stat. Comput., 27 (2017), pp. 1555–1584.
[18] M. M. Dunlop and A. M. Stuart, *The Bayesian formulation of EIT: Analysis and algorithms*, Inverse Probl. Imaging, 10 (2016), pp. 1007–1036, https://doi.org/10.3934/ipi.2016030.
[19] I. Ekeland and R. Temam, *Convex Analysis and Variational Problems*, Classics Appl. Math. 28, SIAM, Philadelphia, 1999.
[20] H. Garde and K. Knudsen, *3D reconstruction for partial data electrical impedance tomography using a sparsity prior*, in Proceedings of the 10th AIMS Conference on Dynamical Systems, Differential Equations and Applications (2014), American Institute of Mathematical Sciences, Springfield, MO, 2015, pp. 495–504, https://doi.org/10.3934/proc.2015.0495.
[21] H. Garde and K. Knudsen, *Sparsity prior for electrical impedance tomography with partial data*, Inverse Probl. Sci. Eng., 24 (2016), pp. 524–541.
[22] H. Garde and S. Staboulis, *The regularized monotonicity method: Detecting irregular indefinite inclusions*, Inverse Probl. Imaging, 13 (2019), pp. 93–116, https://doi.org/10.3934/ipi.2019006.
[23] Matthias Gehre, Bangti Jin, and Xiliang Lu, *An analysis of finite element approximation in electrical impedance tomography*, Inverse Problems, 30 (2014), 045013.
[24] P. F. Grant and M. M. Lowery, *Effect of dispersive conductivity and permittivity in volume conductor models of deep brain stimulation*, IEEE Trans. Biomed. Eng., 57 (2010), pp. 2386–2393.
[25] H. Griffiths, *Magnetic induction tomography*, Meas. Sci. Tech., 12 (2001), pp. 1126–1131.
[26] O. S. Haddadin and E. S. Ebbini, *Ultrasonic focusing through inhomogeneous media by application of the inverse scattering problem*, J. Acoust. Soc. Amer., 104 (1998), pp. 313–325.
[27] B. Harrach and M. Ullrich, *Monotonicity-based shape reconstruction in electrical impedance tomography*, SIAM J. Math. Anal., 45 (2013), pp. 3382–3403.
[28] B. Harrach and M. Ullrich, *Resolution guarantees in electrical impedance tomography*, IEEE Trans. Med. Imaging, 34 (2015), pp. 1513–1521.
[29] B. Jin, T. Khan, and P. Maass, *A reconstruction algorithm for electrical impedance tomography based on sparsity regularization*, Internat. J. Numer. Methods Engrg., 89 (2012), pp. 337–353.
[30] M. A. Kemp, M. Franzi, A. Haase, E. Jongewaard, M. T. Whittaker, M. Kirkpatrick, and R. Sparr, *A high Q piezoelectric resonator as a portable VLF transmitter*, Nat. Commun., 10 (2019), 1715.
[31] R. V. Kohn and A. McKenney, *Numerical implementation of a variational method for electrical impedance tomography*, Inverse Problems, 6 (1990), pp. 389–414.

[32] A. Korzhenevskii and V. Cherepenin, *Magnetic induction tomography*, J. Commun. Technol. Electron., 42 (1997), pp. 469–474.
[33] X. Li, S. K. Davis, S. C. Hagness, D. W. Van der Weide, and B. D. Van Veen, *Microwave imaging via space-time beamforming: Experimental investigation of tumor detection in multilayer breast phantoms*, IEEE Trans. Microwave Theory Techniq., 52 (2004), pp. 1856–1865.
[34] R. Merwa, K. Hollaus, O. Biro, and H. Scharfetter, *Detection of brain oedema using magnetic induction tomography: A feasibility study of the likely sensitivity and detectability*, Physiol. Meas., 25 (2004), pp. 347–354.
[35] R. Merwa, K. Hollaus, B. Brandstätter, and H. Scharfetter, *Numerical solution of the general 3D eddy current problem for magnetic induction tomography (spectroscopy)*, Physiol. Meas., 24 (2003), pp. 545–554.
[36] P. D. Mountcastle, N. A. Goodman, and C. J. Morgan, *Generalized adaptive radar signal processing*, in Proceedings of the 25th Army Science Conference, Defense Technical Information Center, Fort Belvoir, Fairfax County, VA, 2008.
[37] S. L. Penny, *Inspection Techniques for Determining Graphite Core Deterioration for Nuclear Applications*, PhD Thesis, The University of Manchester, Manchester, England, United Kingdom, 2016.
[38] A. Peyton, M. Beck, A. Borges, J. De Oliveira, G. Lyon, Z. Yu, M. Brown, and J. Ferrerra, *Development of electromagnetic tomography (EMT) for industrial applications. Part 1: Sensor design and instrumentation*, in 1st World Congress on Industrial Process Tomography, Buxton Press, Buxton, England, 1999, pp. 306–312.
[39] V. S. Ryaben'kii and S. V. Tsynkov, *A Theoretical Introduction to Numerical Analysis*, Chapman and Hall/CRC, Boca Raton, FL, 2006.
[40] D. S. Shumakov, A. S. Beaverstone, and N. K. Nikolova, *Optimal illumination schemes for near-field microwave imaging*, Progr. Electromagn. Res., 157 (2016), pp. 93–110.
[41] E. Somersalo, M. Cheney, and D. Isaacson, *Existence and uniqueness for electrode models for electric current computed tomography*, SIAM J. Appl. Math., 52 (1992), pp. 1023–1040.
[42] J. A. Stratton, *Electromagnetic Theory*, Wiley, Hoboken, NJ, 2007.
[43] A. Tamburrino, *Monotonicity based imaging methods for elliptic and parabolic inverse problems*, J. Inverse Ill-Posed Probl., 14 (2006), pp. 633–642.
[44] A. Tamburrino and G. Rubinacci, *A new non-iterative inversion method for electrical resistance tomography*, Inverse Problems, 18 (2002), pp. 1809–1830.
[45] A. Tamburrino, G. Rubinacci, M. Soleimani, and W. Lionheart, *A noniterative inversion method for electrical resistance, capacitance and inductance tomography for two phase materials*, in Proceedings of the 3rd World Congress on Industrial Process Tomography, Banff, Canada, Virtual Centre for Industrial Process Tomotraphy, Leeds, England, 2003, pp. 233–238.
[46] M. Tanter, J.-F. Aubry, J. Gerber, J.-L. Thomas, and M. Fink, *Optimal focusing by spatio-temporal inverse filter. I. Basic principles*, J. Acoust. Soc. Amer., 110 (2001), pp. 37–47.
[47] A. N. Tikhonov, A. Goncharsky, V. Stepanov, and A. G. Yagola, *Numerical Methods for the Solution of Ill-posed Problems*, Math. Appl. 328, Springer, Dordrecht, The Netherlands, 2011.
[48] M. Tong Harris, M. H. Langston, P.-D. Letourneau, G. Papanicolaou, J. Ezick, and R. Lethin, *Fast large-scale algorithm for electromagnetic wave propagation in 3D media*, in 2019 IEEE High Performance Extreme Computing Conference (HPEC), IEEE, Piscataway, NJ, 2019.
[49] G. Uhlmann, *Electrical impedance tomography and Calderón's problem*, Inverse Problems, 25 (2009), 123011.
[50] F. Vico, L. Greengard, and M. Ferrando, *Fast convolution with free-space Green's functions*, J. Comput. Phys., 323 (2016), pp. 191–203.
[51] F. Vignon, J. de Rosny, J.-F. Aubry, and M. Fink, *Optimal adaptive focusing through heterogeneous media with the minimally invasive inverse filter*, J. Acoust. Soc. Amer., 122 (2007), pp. 2715–2724.
[52] W. Yang and L. Peng, *Image reconstruction algorithms for electrical capacitance tomography*, Meas. Sci. Tech., 14 (2002), R1.